NUCLEAR MAGNETIC RESONANCE MICROSCOPY OF NAFION®-117 PROTON EXCHANGE POLYMER MEMBRANES

by

Daniel Trusler Howe

A thesis submitted in partial fulfillment
of the requirements for the degree

of

Master of Science

in

Chemical Engineering

MONTANA STATE UNIVERSITY
Bozeman, Montana

November 2004

© COPYRIGHT

by

Daniel Trusler Howe

2004

All Rights Reserved

APPROVAL

of a thesis submitted by

Daniel Trusler Howe

This thesis has been read by each member of the thesis committee and has been found to be satisfactory regarding content, English usage, format, citations, bibliographic style, and consistency, and is ready for submission to the College of Graduate Studies.

Dr. Joseph Seymour

Approved for the Department of Chemical and Biological Engineering

Dr. Ronald W. Larsen

Approved for the College of Graduate Studies

Dr. Bruce McLeod

STATEMENT OF PERMISSION TO USE

In presenting this thesis in partial fulfillment of the requirements for a master's degree at Montana State University, I agree that the Library shall make it available to borrowers under rules of the Library.

If I have indicated my intention to copyright this thesis by including a copyright notice page, copying is allowable only for scholarly purposes, consistent with "fair use" as prescribed in the U.S. Copyright Law. Requests for permission for extended quotation from or reproduction of this thesis in whole or in parts may be granted only by the copyright holder.

Daniel Trusler Howe

November 2004

TABLE OF CONTENTS

1. INTRODUCTION 1

Fuel Cells 1
Basic Operating Principles 1
Proton Exchange Membranes 3
Restricted Diffusion 6
Nuclear Magnetic Resonance 9
Fundamental Concepts 10
Energy Levels 11
Net Magnetization 12
Angular Momentum 14
The Rotating Frame 16
Excitation 17
Relaxation 18
NMR Signal Detection 19
Magnetic Resonance Microscopy 22
Gradients 22
Spin Echoes 23
k-space 24
2-D imaging 25
Image Resolution and Limitations 27
Thesis Goal 29

2. MATERIALS AND METHODS 30

Nafion-117 30
Sample Preparation 30
MRM Apparatus 32
MRM Experimental Procedure 33
T_2 Images 33
Constructing T_2 Maps 35
Diffusion Images 37
Constructing Diffusion Maps 39
Membrane Heterogeneity Experimental Scheme 41
Membrane Sampling Procedure 41
Experimental Setup 42

3. RESULTS AND DISCUSSION 44

Solvent Mobility as a Function of Methanol Concentration 44

TABLE OF CONTENTS – CONTINUED

T_2 Measurements 44
Diffusion Measurements 55
Material Inhomogeneity 63

4. CONCLUSIONS 67

LITERATURE CITED 69

LIST OF FIGURES

Figure Page

1.1. Fuel Cell Schematic 2

1.2. Graphical Representation of Restricted Diffusion 8

2.1. Dilution Chart for 24 Hour Hydration Soak 31

2.2. Pulse Program for T_2 Mapping 35

2.3. Graphical Method for Calculating T_2 Values 36

2.4. Pulse Program for Diffusion Mapping 39

2.5. Sample Stejskal-Tanner Plot of Diffusion Data 40

2.6. Punch Scheme for Material Inhomogeneity Experiment 41

3.1. T_2 Maps for the Various Methanol Concentrations 45

3.2. T_2 Averages 48

3.3. Average T_2 Values of the Free Liquid 51

3.4. Average T_2 Values of the Liquid Within the Membranes 52

3.5. Membrane Swelling via T_2 Measurements 53

3.6. Diffusion Maps for the Various Methanol Concentrations 55

3.7. Diffusion Coefficient Averages 57

3.8. Average Self-Diffusion Coefficients Within the Free Liquid 59

3.9. Average Diffusion Coefficients of the Liquid Within the Membrane 60

3.10. Membrane Swelling via Diffusion Measurements 61

3.11. Quantitative Measurements of Membrane Swelling 62

LIST OF FIGURES - CONTINUED

3.12. T_2 Maps for Two Samples Prepared Separately 64

3.13. Longitudinal T_2 Maps for Material Inhomogeneity Study 65

3.14. Transverse T_2 Maps for Material Inhomogeneity Study 65

ABSTRACT

As the combustion of fossil fuels for the generation of energy and transportation becomes more expensive, of limited supply, and environmentally unsound, the development of viable fuel cell alternatives becomes more important. A comprehensive understanding of the proton exchange membranes (PEM's) used as electrolytes in certain types of fuel cells will play a major role in bringing the cost and reliability of PEM fuel cell systems down to a competitive level with traditional fossil fuel methods. Magnetic resonance microscopy (MRM) is well suited to the study of these membranes because it is non-invasive, and can spatially resolve material structure and give data on transport phenomena such as diffusion that cannot be determined by other methods. The goal of this research was to use magnetic resonance microscopy to study solvent mobility levels within the polymer membranes via spin-spin, T_2, magnetic relaxation and diffusion mapping. The molecular mobility can quantify membrane swelling and spatial heterogeneity of the membrane material. A key aim of the research is to correlate these findings with previous bulk MRM studies of solvent within polymer membranes. Prior bulk MRM studies of solvent molecular mobility at different hydration levels were unable to study the membranes fully submersed in solvents, as the free solvent signal would dominate the nuclear magnetic resonance (NMR) signal from the solvent within the membrane. In this study spatial resolution of the MRM data provides the means to study fully saturated membranes, a condition of interest since the degree of hydration is related to membrane operational efficiency. The material homogeneity of the polymer in the thickness and surface directions of the membrane, an important factor in the reliable performance of fuel cells, was studied via T_2 mapping. Nafion®-117 was the proton exchange membrane studied because it is currently the most popular electrolyte used in the PEM fuel cell industry and several bulk MRM studies have been conducted. Results indicate that both solvent mobility and membrane swelling are highly dependant on the concentration of methanol used to prepare the samples, as seen in the bulk studies, and that solvent mobility can vary on the 20 micron level within the polymer in both the thickness and surface directions. This research establishes MRM as an important tool for the study of individual proton exchange polymer membrane samples and provides a basis for extension to the study of membranes during operation.

INTRODUCTION

Fuel Cells

Basic Operating Principles

A fuel cell is an electrochemical device that converts chemical energy directly into electricity. Its only inputs are hydrogen and oxygen (usually in the form of air) and the only outputs are heat and water. With the need for energy systems that are not dependent on fossil fuels skyrocketing, turmoil in the areas that produce the majority of these fossil fuels, and environmental concerns about the effects of combusting them, fuel cell systems have seen remarkable attention in the last two decades [1].

The electrochemistry of a hydrogen fuel cell is very simple. Pure hydrogen is fed to an anode loaded with a platinum catalyst. The hydrogen is ionized according to the equation $2H_2 \rightarrow 4H^+ + 4e^-$. The hydrogen ions formed at the anode will pass through the proton exchange polymer membrane electrolyte, and the electrons will travel through an external circuit. On the other side of the fuel cell, oxygen, usually in the form of air, is fed to a cathode also loaded with a platinum catalyst. As the hydrogen ions pass through the membrane and the electrons reach the cathode, they will recombine with the oxygen according to the equation $O_2 + 4e^- + 4H^+ \rightarrow 2H_2O$. This process generates only waste heat,

water, and an electrical current. The heat is removed from the anode side, and the waste water passes out of the fuel cell from the cathode side [2]. Figure 1.1 shows the basic operating principles of a proton exchange membrane fuel cell [3].

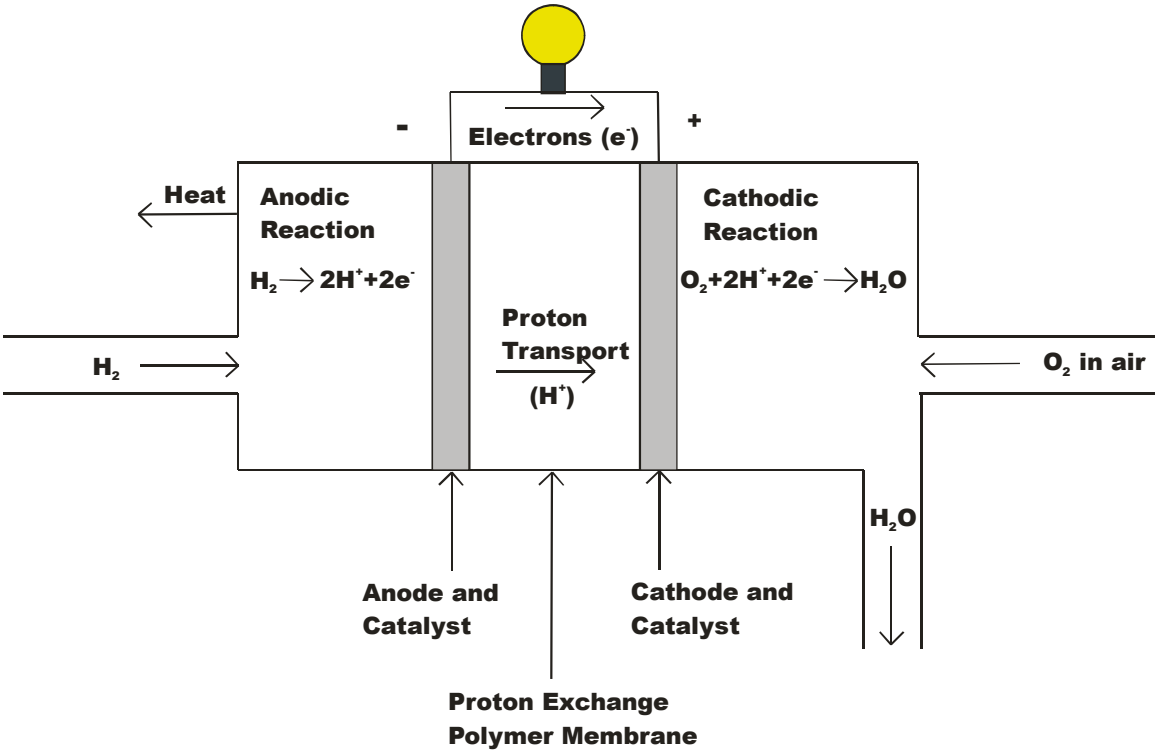


Figure 1.1 Schematic showing the basic operating principles of a proton exchange membrane fuel cell (PEMFC). Hydrogen is fed to the anode and oxygen is fed to the cathode. The electrons pass through an external circuit, lighting the bulb, while the hydrogen ions pass through the proton exchange membrane. On the cathode side the hydrogen ions, electrons, and oxygen recombine to form water, which is passed out of the fuel cell.

Proton Exchange Membranes

One of the greatest challenges facing the commercial viability of PEMFC's is the development of a suitable membrane for use as the electrolyte. The ideal membrane will completely repel electrons while being an excellent conductor of the hydrogen ions. The most widespread proton exchange polymer membrane used today is Nafion®, manufactured by DuPont. Nafion® was first developed in the early 1960's by grafting sulfonic acid groups onto a polytetrafluoroethylene (PTFE) backbone. Previous studies had attempted to use polystyrene sulfonic acid polymers as an electrolyte in fuel cells, but the oxidative environment present at the cathode was resulting in premature failure of the membrane. PTFE, unlike polystyrene, is totally chemically inert, so by using it as a backbone the chemical instability of polystyrene was avoided [4].

While the chemical stability of Nafion® is necessary for the environment it encounters, there are drawbacks to its use as an electrolyte. It is extremely rigid, which limits the possible geometries of the fuel cell designs. Even more limiting is its poor proton conductivity unless properly hydrated [5]. The dry polymer consists of individually isolated spherical ionic clusters. These are the sulfonate ions derived from the sulfonic acid groups grafted onto the inert PTFE backbone, and they generally have a diameter around 15Å. The space between the ionic clusters is approximately 27Å [6].

As the Nafion® begins to absorb water the membrane will start to swell. At a water volume fraction of 0 to 0.2, the clusters will become spherical pools of water where the ionic groups are located at the polymer/water boundary. The diameter of the pools is 20Å, but the separation between the pools is 30Å [6].

As the membrane continues to absorb water, the clusters will continue to swell. From 0.2 to 0.3 volume fraction water the cluster diameter will increase to 40Å, although the inter-cluster distance remains approximately the same. This is due to an increase in the number of ionic groups per cluster, known as percolation. This also results in a decrease in the total number of clusters present. At this point the ionic conductivity of the polymer will increase sharply [6].

From 0.3 to 0.5 volume fraction water the ionic clusters will form connecting cylinders of water between them. The cluster diameter increases to 50Å. Although the size of these connecting cylinders is not precisely known, the increasing ionic conductivity suggests that both the length and diameter of the channels are also increasing [6].

Above 0.5 volume fraction water, a structural inversion occurs. A rod-like structure will emerge, consisting of polymer aggregates. The hydrophobic phase consisting of the entangled PTFE chains will be rigid, while the hydrophilic phase consisting of the water and ionic groups will be relatively fluid. Although maintaining a spherical geometry would be energetically more beneficial, the packing constraints of the swelling polymer will not allow it [6].

Between 0.5 and 0.9 volume fraction water the entire connected network will begin to swell. This swelling is caused by an increase in the distance between the ionic groups as the amount of water increases and a partial dissolution of the membrane itself. The result is a colloidal dispersion of the rods, which can act as “flow channels” for the hydrogen protons [6,7]. A fully hydrated sample of Nafion® can reach a proton conductivity of 0.1 S cm^{-1} [8], but simply placing the Nafion® in water will not produce adequate hydration. The most successful method for achieving hydration found thus far is to employ a solution of methanol and water. The solvent uptake levels, and thus the overall hydration levels, are considerably higher for a water/methanol system than for pure water [9].

Another issue of vital importance to the fuel cell industry is material inhomogeneity. The most widely used member of the Nafion® family is Nafion-117®, which has a thickness of 0.177 mm and an equivalent weight of 1100 grams [10]. Nafion-117® is produced as an extrusion-cast membrane. This allows high speed, high volume, automated manufacturing facilities, resulting in a much less expensive material [4]. This rolling procedure, however, results in mechanical stresses and strains inherent in the final product. When the polymer is hydrated these inconsistencies will lead to uneven hydration across the membrane. Uneven hydration can result in poor performance and possible point failures when the polymer is used in a fuel cell [11].

Restricted Diffusion

The evolution of the flow channels used to transport the hydrogen protons through the polymer, as seen in the preceding section, necessitates a discussion on restricted diffusion. For a liquid or gas in a relatively large sample container diffusion will be a random process, with the macroscopic direction of the flow determined by Fick's first law of diffusion. When diffusing through a pore or capillary, however, the walls of the channel will impose boundaries on the diffusive behavior. The tighter the pore, the more restricted the possible motion and the greater the effect the walls will have on the diffusion process.

Consider a single particle within a capillary of diameter L. When studying diffusion it is not the velocity of the particle that is of interest but rather the variation in particle position. This variation is given by the Einstein relation, shown here as

$$<Z^2(t)> = 2\ D(t)\ t \qquad (1.1),$$

where Z is the particle position, t is the time, and $D(t)$ is the time dependent diffusion coefficient. At equilibrium the variance and diffusion coefficients will no longer be functions of the time scale, but the equation given above will work for all times. Within the pore the diffusion time scale will be defined as the time it takes to sample the entire length of the capillary diameter by diffusion: L^2/D_o. D_o is the free diffusion coefficient, measured in a sample where boundary effects are negligible. Now if t is much less than the diffusion time scale, the diffusive

motion will resemble free diffusion because most of the particles will not have interacted with the capillary wall. The ratio of $D(t)/D_o$ will approach one. As *t* increases, however, the pore boundaries will begin to interact with the particles. When *t* is much greater than the diffusion time scale the pore space will be sampled completely, and the $D(t)/D_o$ ratio will decrease toward an asymptotic restricted diffusion value. In this region the variance is purely a function of the pore size, and the Einstein relation simplifies to

$$\langle Z^2 \rangle = L^2 \qquad (1.2).$$

In many diffusion experiments via NMR the restricted diffusion coefficient is the value of interest, and consequently it is only necessary to take readings after the equilibrium value has been established. However, by running time dependent diffusion studies the diameter of the pore in question can be ascertained by applying the Einstein relation after it has been solved for the pore diameter, namely

$$L_{app} = (2\, D_{exp}\, t)^{1/2} \qquad (1.3).$$

This relation can be used to correlate the pore sizes mentioned in the Gebel paper [6]. The mechanics of restricted diffusion are shown in figure 1.2 [12].

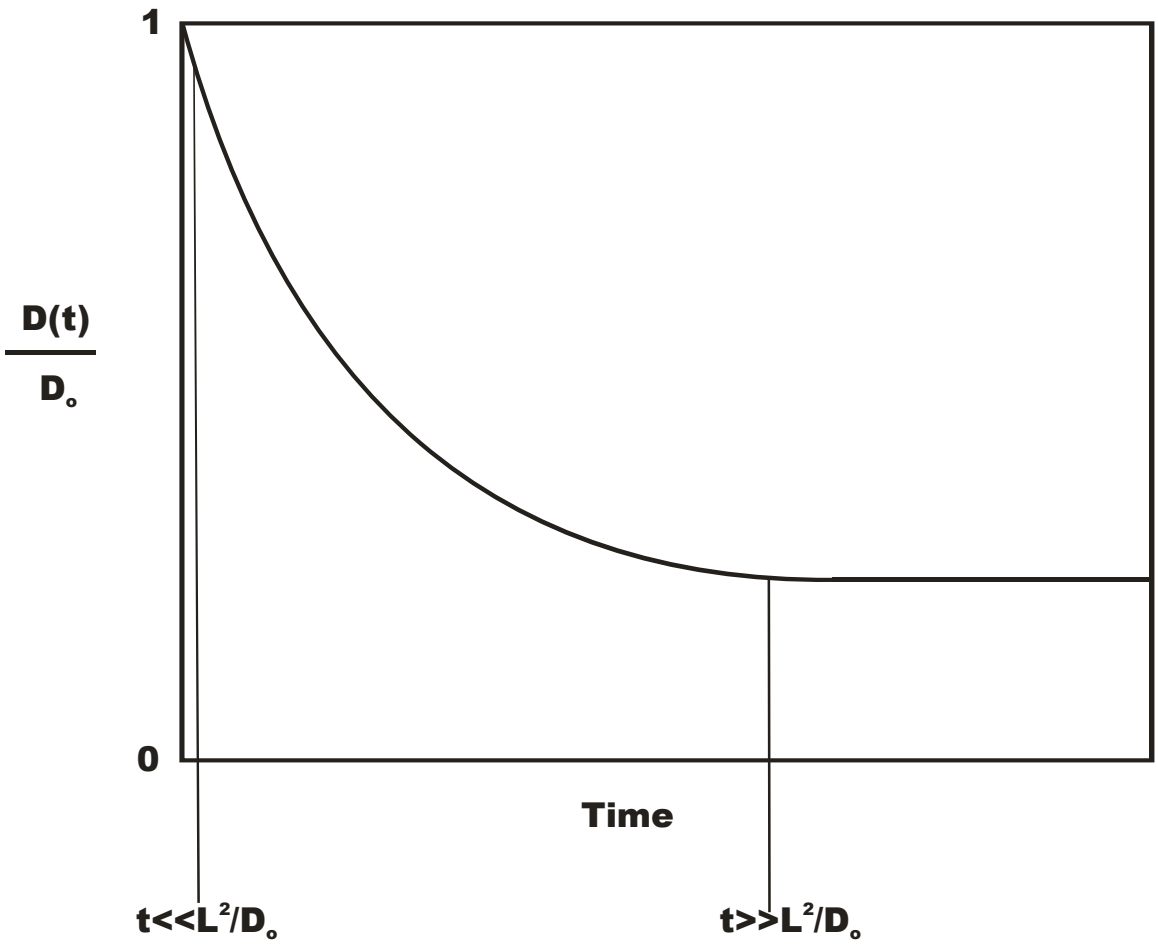


Figure 1.2 Graphical representation of restricted diffusion. The graphed line is equal to L^2/D_{exp}. For times much less than the diffusion time scale the observed motion will resemble that of free diffusion. At long times the value of the diffusion coefficient will be that for restricted diffusion. The transient period in between the two time scales allows for calculation of the pore size through the Einstein relation [12].

Magnetic resonance microscopy (MRM) is extremely well suited to studying the material properties discussed above. Since MRM is non-invasive it can study polymer samples in exactly the same state as they would be used in a fuel cell, and it can also probe at any depth into the membrane. Until now, most MRM investigations have focused on either the bulk properties of Nafion® [13,14]

or on the electrophoretic effects such as electroosmotic drag and electrical mobility of the charge carriers [15,16]. The hydration levels, material swelling, self-diffusion of the liquids within the polymer, and material homogeneity of individual samples have been largely ignored. In this study the ability of MRM to precisely determine boundaries between free liquid and a solid has allowed the quantitative determination of swelling effects. It also allows the hydration levels to be determined as a function of the concentrations of methanol used in the preparation. Diffusion within the membrane and material consistency of individual samples can also be observed with reasonably high spatial resolution, namely 19.5 μm/pixel.

Nuclear Magnetic Resonance

The following section gives a general summary of the physics that underlie the nuclear magnetic resonance phenomenon. If a more thorough understanding of the subject is required the texts by Abragham [17] and Schlichter [18] give a detailed explanation of the quantum mechanical theory behind many of the principles and derivations. Some other useful NMR texts used in the following section are Callaghan [19], Codd [20], and Farrar [21].

Fundamental Concepts

Most chemical compounds of interest to chemists and engineers are magnetically neutral in a macroscopic sense. However, when placed in a large external magnetic field, the magnetic properties of the nucleus will result in a macroscopic magnetic moment for the sample. This leads to the term nuclear magnetic resonance. This theory was proven when the magnetic properties of solid hydrogen were first demonstrated in 1937 by Lasarew and Schubnikow[21].

In order for a sample to exhibit a macroscopic magnetic moment the nuclei must be aligned in a specific direction. Without a magnetic field the nuclei will arrange themselves at random, resulting in zero magnetic moment. In a large DC magnetic field, however, the nuclei prefer to align themselves with the field rather than against it. This preferential direction corresponds to the lower energy state of magnetic moments aligned with the magnetic field. Those nuclei aligned against the field will have a higher energy state, and thus two concrete energy levels will be exhibited. In order for the sample to have a net magnetic moment there must be more nuclei in one energy state than in the other. The Boltzman distribution allows for a slightly higher population of spins in the lower energy state than in the higher state [18]. Although the difference may be small, on the order of parts per million, the large number of spins in a small liquid sample will result in a statistically significant macroscopic difference. Accomplishing this population difference requires that the nuclei exchange energy with the sample.

Some of the first successful NMR experiments were dedicated to proving that this energy exchange did in fact take place. In 1946 Purcell, Torrey, and Pound used solid paraffin as a sample and were able to measure the resonance absorption of the protons. Using a radio frequency bridge circuit tuned to the resonance frequency of the protons they were able to quantify the proton energy loss caused by the energy absorption of the sample [21]. Working independently in the same year, Bloch, Hansen, and Packard measured the signal induced by the precession of the magnetic moments in a tuned radio frequency circuit for a water sample [21]. Both experiments helped prove the fundamentally important theory of energy exchange between the nuclei and the sample lattice. They also showed the direction of energy flow, namely that at thermal equilibrium energy will pass from the nuclei to the sample lattice, resulting in a higher population of nuclei in the lower energy state.

Energy Levels

Any given particle will have a spin quantum number, I, associated with it. This number will be an integer or half integer, such as 1 or ½. For an isolated nucleus with spin I, the possible energy levels will be equal to $2*I + 1$. These energy levels will be equally spaced by a distance ΔE, given by [21]

$$\Delta E = \mu \mathbf{B_0}/I \qquad (1.4).$$

Here μ is the nuclear magnetic moment and $\mathbf{B_o}$ is the applied magnetic field. The nuclear magnetic moment is what allows the nucleus to interact with a magnetic field. It is given by [21]

$$\mu = \gamma h I / 2\pi = \gamma \hbar I \qquad (1.5).$$

In this equation γ is the gyromagnetic ratio, which is always constant for a given nucleus. Planck's constant, *h*, is equal to 6.626 X 10^{-34} J*s. The variable $\hbar$ is equal to $h/2\pi$.

In order for a transition to occur from one energy level to the next adjacent energy level, a particle must absorb energy at a specific frequency. This frequency, ω_o, is derived from the Bohr relation and is given by [21]

$$\omega_o = \gamma \mathbf{B_o} \text{ (rad/sec)} \qquad (1.6),$$

with ω_o known as the Larmor frequency. Application of energy at this frequency will result in absorption by the particle and a consequent jump between energy levels. The particle will be said to resonate at this frequency. Equation 1.6 gives the dependence of the Larmor frequency on the strength of the magnetic field the nucleus experiences, and is perhaps the single most important equation in nuclear magnetic resonance.

Net Magnetization

Magnetization, on a molecular scale, is an extremely fast process. A magnetization vector's orientation can be changed in less than a microsecond,

and some processes such as spin-coupling effects and nuclear magnetic energy levels can be switched on or off almost instantly. For example, if a sample of water were placed in a DC magnetic field the two discrete energy levels mentioned earlier would be attained effectively instantly. These near-instantaneous processes are called nuclear magnetization processes.

In many cases the individual microscopic properties are not as important as the overall effect that these properties have on the sample as a whole. Take, for example, the macroscopic magnetic moment of a sample. This is defined as the sum of all the microscopic moments, and is given by [21]

$$\mathbf{M} = N\gamma^2\hbar^2 I\,(I+1)\,\mathbf{B_o} / 3kT \qquad (1.7),$$

where N is the total number of proton spins, I is the spin quantum number, k is the Boltzman constant, and T is the absolute temperature measured in degrees Kelvin.

At equilibrium the ratio of spins in the lower energy state, N_+, and the upper energy level, N_-, can be given by the Boltzman relation [21]

$$N_+ / N_- = \exp(\Delta E / kT) \qquad (1.8).$$

If the system is in equilibrium the population difference between the two energy levels will be given by the Boltzman equation [21]

$$\Delta N = (N_+ - N_-) \approx N\,\Delta E / 2\,k\,T \approx N\,\mu\,\mathbf{B_o} / 2\,k\,T \qquad (1.9).$$

For this system there will be more nuclei in the lower energy state than in the higher energy state, and ΔN will be positive. This results in the net magnetic moment $\mathbf{M}$ being a positive vector aligned with the magnetic field, and

calculations for each individual spin are no longer necessary. Consequently the macroscopic magnetic moment of the sample can now be used to adopt a classical mechanics approach rather than the quantum mechanical description used up to this point.

Angular Momentum

A spinning proton possesses angular momentum similar in nature to that of a spinning gyroscope. For a gyroscope the magnitude of the angular momentum is a function of its radial size, its mass, and the speed at which it is spinning. The total angular momentum of this gyroscope is related to the linear momentum by [21]

$$\mathbf{J} = \mathbf{r} \times \mathbf{p} = \mathbf{r} \times m\bullet\mathbf{v} = (m\bullet\mathbf{r}) \times \mathbf{v} \qquad (1.10),$$

where $\mathbf{r}$ is the radius of gyration, $\mathbf{p}$ is the linear momentum, m is the mass, and $\mathbf{v}$ is the linear velocity. The time rate of change of $\mathbf{J}$ will be then be given by Newton's second law of motion, resulting in the equation [21]

$$d\mathbf{J}/dt = \mathbf{L} \qquad (1.11),$$

where $\mathbf{L}$ is the torque acting upon the top. It is important to note that the magnitude of $\mathbf{J}$ is a constant when a torque is applied. It is only the direction of $\mathbf{J}$ that varies in time according to equation 1.11.

While the above example is similar to a spinning proton, one of the major differences is that a proton possesses a nuclear magnetic moment.

Consequently a torque will be applied when the proton is placed in a magnetic field. The stronger the magnetic field $\mathbf{B_o}$, the greater the torque. This results in an increasing resonance frequency as the magnitude of the magnetic field increases. The equation describing this interaction is given by [21]

$$\mathbf{L} = \mu \times \mathbf{B_o} \qquad (1.12).$$

Here μ is the magnetic moment of the nucleus, which is a physical constant. It is defined as [21]

$$\mu = \gamma \bullet \mathbf{J} \qquad (1.13).$$

Substituting (1.9) into equation (1.8) results in

$$d\mathbf{J}/dt = \mu \times \mathbf{B_o} \qquad (1.14).$$

This can also be stated as

$$d\mu/dt = \gamma(d\mathbf{J}/dt) = \gamma(\mu \times \mathbf{B_o}) \quad (1.15).$$

For a given NMR experiment the magnetic field will be held constant, and the magnetic moment of the nucleus is also a constant. Hence the magnetic moment will precess, or resonate, at a constant frequency about the direction of the magnetic field. This frequency is called the Larmor frequency, and was given in equation (1.6). Since the gyromagnetic ratio is both constant and known, the Larmor frequency can be calculated for any magnetic field strength.

The Rotating Frame

As seen in the previous section, a proton placed in a magnetic field will precess about $\mathbf{B_o}$ at the Larmor frequency. At equilibrium there are more nuclei aligned with the magnetic field, and thus the net magnetization moment, $\mathbf{M}$, will be parallel to the magnetic field. If the magnetic field is applied along the *Z* axis in Cartesian coordinates, the resulting magnetization will also be aligned along the *Z* axis. The *X* and *Y* components will be zero since the magnetization is entirely aligned along *Z*. If the field is static, the *Z* component of the net magnetization will be constant.

To achieve resonance another magnetic field, $\mathbf{B_1}$, is applied in the plane perpendicular to $\mathbf{B_o}$, called the transverse plane. This magnetic field oscillates at the Larmor frequency and thus varies with time. The resulting net magnetic field will be the sum of $\mathbf{B_o}$ and $\mathbf{B_1}$. In order to simplify the mathematics it is convenient to define the coordinate system as one that rotates around $\mathbf{B_o}$ at the frequency ω_o. This is known as the rotating frame. The new axes will be denoted *X*', *Y*', and *Z*'. Since $\mathbf{B_o}$ is constant and the precession about it is constant this has the effect of removing the $\mathbf{B_o}$ term from the mathematics entirely. The result is that $\mathbf{M}$ will precess only about $\mathbf{B_1}$ at the frequency given by

$$\omega_1 = \gamma \mathbf{B_1} \text{ (rad/sec)} \qquad (1.16).$$

The rotating frame can be likened to that almost always used on the planet Earth. Even though the Earth is rotating about the sun at over 1000 miles

per hour while spinning on its axis, it is customary to refer to a position on Earth as “stationary”. By doing so a rotating frame is assumed that is similar to that used in the NMR lab. In this frame an arrow shot into the air would go straight up and come straight back down. To a distant observer, however, the arrow’s behavior would be considerably more complicated.

Excitation

For a sample in a static magnetic field applied along the *Z* axis, **M** will remain stationary along the *Z*’ axis. When a radio frequency (rf) pulse is applied to a sample at the Larmor frequency, ω_o, the magnetic moment **M** will precess about $\mathbf{B_1}$ through an angle given by [21]

$$\Theta = \gamma \mathbf{B_1} t \text{ (rad)} \qquad (1.17).$$

Here Θ is the flip angle, and *t* is the duration of the applied rf pulse. A flip angle equal to 180° results in the magnetization moving from the *Z* direction to the –*Z* direction, while a 90° angle gives magnetization only in the transverse (*X,Y*) plane. This 90° rf pulse application is known as “excitation”. The pulse will also be characterized by the axis along which it is applied. If a pulse is applied along the *Y*’ axis it will flip the signal entirely along the *X*’ axis. The pulse will thus be designated by the flip angle subscripted with the axis. An excitation pulse along the *Y*’ axis would be designated $90°_Y$. By carefully choosing the $\mathbf{B_1}$ axis and the

duration of the pulse, the position of $\mathbf{M}$, and thus the signal acquired, can be manipulated.

Relaxation

A sample at thermal equilibrium will exhibit nuclei distributed among the energy levels according to the Boltzman distribution. Excitation occurs when a sample absorbs energy from an rf pulse at the Larmor frequency. When the pulse is no longer applied the system will begin returning to the equilibrium state. It accomplishes this by exchanging thermal energy with its surroundings, known as "the lattice" [19]. This leads to the term spin-lattice relaxation. As the energy exchange precedes, the longitudinal magnetization, $\mathbf{M_Z}$, will return to the equilibrium value $\mathbf{M_o}$. The time rate of change of this process is a function of both $\mathbf{M_o}$ and the spin-lattice relaxation time constant, denoted T_1. T_1 times may vary widely, usually over a range of 10^{-4} to 10^4 seconds, but for a small diamagnetic system with a spin ½ nucleus it is usually on the order of 0.1 to 10 seconds [19]. The time rate of change is given by

$$d\mathbf{M_Z}/dt = -(\mathbf{M_Z} - \mathbf{M_o}) / T_1 \qquad (1.18),$$

and the solution to this equation is given by

$$\mathbf{M_Z}(t) = \mathbf{M_Z}(0)\exp(-t / T_1) + \mathbf{M_o}[1 - \exp(-t / T_1)] \qquad (1.19).$$

While the longitudinal relaxation seen above is an important process in MRM experiments, the transverse relaxation is also extremely important.

Transverse relaxation occurs when the spins come to thermal equilibrium by exchanging energy amongst themselves. The transverse magnetization is caused by phase coherence, and in order to return to an equilibrium state of zero transverse magnetization the spins must dephase. This process is known as spin-spin relaxation, and is characterized by the time constant T_2. The time rate of change is given by the equation

$$d\mathbf{M}_{XY}/dt = -\mathbf{M}_{XY} / T_2 \qquad (1.20),$$

and the solution is given by

$$\mathbf{M}_{XY}(t) = \mathbf{M}_{XY}(0)\exp(-t / T_2) \qquad (1.21).$$

The equation above applies when the interactions causing transverse relaxation are weak. For solids and large molecules undergoing extremely slow motions the decay will be much more complicated than that described in equation (1.21). However, for the slowly relaxing liquid systems studied in this report the T_2 determination approach outlined above is perfectly appropriate.

NMR Signal Detection

The excitation of the nuclear spins by an applied rf pulse results in the precession of $\mathbf{M}$ in the transverse direction at the frequency emitted by the spins. This rotation will result in an induced current in the coils used to deliver the original rf pulse, and the current induced can be measured. Signal processing will result in the magnetization vectors $\mathbf{M}_X$, which is the real segment of the data,

and $\mathbf{M_Y}$, which is the imaginary component. A complex result is achievable due to the quadrature detection being employed. The use of quadrature detection allows the sign of the frequency to be established, and increases the number of frequencies which can be distinguished [19]. Both the real and imaginary components are combined to give the Free Induction Decay (FID) which is a time-dependent voltage response signal. For a single frequency, which is seen in cases such as pure samples of water or benzene, the FID will be a sinusoidal wave decaying with a rate constant equal to T_2. By measuring the period of the wave the frequency of the signal can be calculated using the relationship that frequency is the inverse of the period. When there are multiple protons present in the sample, however, the FID will contain all of the different frequencies, and such simple relationships cannot be used. Since the FID is in the time domain, and data in the frequency domain is required, a Fourier Transform (FT) of the data becomes necessary. Converting between the frequency domain and the time domain requires the following two equations [22],

$$F(k) = \int f(t)\, e^{-ikt}\, dt \qquad (1.22)$$

$$F(t) = \int f(k)\, e^{ikt}\, dk \qquad (1.23)$$

where *t* is the time domain, k is the frequency domain, $f(t,k)$ is a function in either the time or frequency domain, and $F(t,k)$ is the same function converted into the

Fourier conjugate domain. By applying these equations to an FID all of the frequencies present can be determined.

Because the coils used to measure the signal are extremely sensitive, several steps must be taken to maximize the ratio of actual MRM signal to background thermal noise. The first step is to “tune” and “match” the impedance of the probe circuitry to match that of both the rf transmitter and the signal preamplifier. This results in efficient power transfer and a minimization of the pulse-widths [23]. The second step is to employ signal averaging. Acquiring multiple signals and averaging them will result in a coherent addition of the actual MRM signal. The noise will be incoherent, and will be smoothed out by the averaging process. The signal to noise ratio will increase proportional to the square root of the number of averages taken. A larger number of averages will thus increase the signal to noise ratio, but will also lengthen the duration of the experiment. Many MRM experiments also require a delay time on the order of T_1 to elapse between signal acquisitions in order to ensure adequate relaxation of the sample to minimize artifacts due to signal from previous excitations [19]. The delay relative to the T_1 value also provides for T_1 weighting of the data.

Magnetic Resonance Microscopy (MRM)

Gradients

As mentioned earlier, careful tuning of the currents within the coils and proper design of the magnets are necessary to remove field inhomogeneities and maximize the signal to noise ratio. One inhomogeneity that can be purposely built into the experiments, however, is the magnetic field gradient. If a second magnetic field designed to vary linearly across the sample space is applied in addition to the static field $\mathbf{B_o}$, then there will be a similar spatial dependence exhibited by the nuclear spins. The Larmor frequencies of the spins will vary linearly according to their location in the sample, and thus the frequencies can be used to determine the location of the spins.

Application of such a field requires special coils, and the applied gradient is always much smaller then the static field $\mathbf{B_o}$. Due to the disparity of magnitudes between the two fields, the Larmor frequency will only show a measurable effect due to the magnetic field perturbation parallel to $\mathbf{B_o}$. All other components will only slightly alter the net field direction. Therefore the local Larmor frequency can be defined mathematically as [19]

$$\omega(\mathbf{x}) = \gamma\mathbf{B_o} + \gamma\mathbf{G}\bullet\mathbf{x} \qquad (1.24),$$

where ω is the spatially dependant frequency, γ is the gyromagnetic ratio, and $\mathbf{G}$ represents the gradient field component parallel to $\mathbf{B_o}$ [19].

Spin Echoes

The physics of NMR are reversible, in the sense that the coil used to deliver an rf pulse to a sample is the same coil that will measure the induced signal. There is a finite amount of time, however, when the switchover from transmitter to receiver takes place. If a pulse is delivered and a gradient applied to the sample, there will be a period at the start of the experiment where measurements cannot be made due to this switchover. Spin echoes are used to overcome this hardware limitation and gain information about the beginning of the experiment [24].

The use of field gradients results in nuclear spins resonating at different Larmor frequencies dependant on their position in the sample. These spins are responsible for a magnetic field equal to $\Delta\mathbf{B_o}$ spread across the sample. The transverse magnetization following a $90°_x$ pulse will be dephased due to this field, and will last for a period of time on the order of $(\gamma\Delta\mathbf{B_0})^{-1}$. This loss of phase coherence is another of the important reversibilities inherent in MRM studies. If a 180° pulse is applied to the sample after a time delay τ has passed then the gradient effects will be reversed. At time 2τ the original signal will be recovered, and information about the initial phase of the experiment can be recorded [19].

k-space

For a given volume element dV within a sample the spin density of that element can be represented as $\rho(\mathbf{r})$, and simple multiplication of the two terms will result in the total number of spins within that element. Hence the signal from this element can be written mathematically as [19],

$$dS(\mathbf{G},t) = \rho(\mathbf{r})\, dV \exp[I\ (\gamma \mathbf{B_o} + \gamma\ \mathbf{G}\bullet\mathbf{r})\ t] \qquad (1.25)$$

in which $dS(\mathbf{G},t)$ will be real at the time origin, and thus $\rho(\mathbf{r})$ will be real rather then complex.

The signal defined above will be a difference frequency, due to the actual signal gathered being mixed with a reference signal, a process known as heterodyne mixing. If the reference frequency is the Larmor frequency, the gathered signal with oscillate at $\gamma\mathbf{G}\bullet\mathbf{r}$. This means that the $\gamma\mathbf{B_o}$ term in equation (1.24) is negligible, and the signal amplitude can be expressed as [19]

$$S(t) = \iiint \rho(\mathbf{r}) \exp[\, i\, \gamma \mathbf{G} \bullet \mathbf{r}\ t]\, d\mathbf{r} \qquad (1.26).$$

In this case *dr* is used to represent volume integration. A Fourier transformation can be used to sum the oscillating terms. In order to simplify the concept a reciprocal to space wavelength vector, **k**, is defined as [19]

$$\mathbf{k} = (2\pi)^{-1}\, \gamma\ \mathbf{G}\ t \qquad (1.27).$$

The **k** vector defined above has units of reciprocal space, m^{-1}. Applying the concepts of the Fourier transform will result in the signal amplitude expressed in

terms of this **k**-space, defined as

$$S(\mathbf{k}) = \iiint \rho(\mathbf{r}) \exp[i\, 2\pi \mathbf{k} \bullet \mathbf{r}]\, d\mathbf{r} \qquad (1.28)$$

and the inverse, the spin-density function, will become

$$\rho(\mathbf{r}) = \iiint S(\mathbf{k}) \exp[-i\, 2\pi \mathbf{k} \bullet \mathbf{r}]\, d\mathbf{k} \qquad (1.29).$$

One of the features of *k*-space that makes it so useful for MRM is that it may be traversed either by varying the gradient magnitude or by varying the gradient duration. For most MRM experiments one spatial dimension is accessed by holding the gradient constant and taking a number of samples, N_S, with a successive time increment equal to τ_S. This is called the "read" direction. The higher one samples in *k*-space, the better the image resolution achieved. By moving across *k*-space the spins from multiple volume elements can be sampled.

2-D Imaging

A line is nothing more than a collection of points. In the presence of a magnetic field gradient a collection of signal points can be obtained in a one-dimensional line in *k*-space by sampling the FID at discrete time intervals. This line will be oriented along one of the axes, and the gradient used to obtain this line will be known as the "read" gradient as mentioned above. If a gradient is then applied perpendicular to the read gradient before the sampling period starts then the intercept of the read axis with the orthogonal axis can be manipulated. This second gradient is termed the "phase" gradient, due to the phase

modulation effect it has on the signal, and it allows for spatial resolution in a second direction. If the read gradient is defined as being in the *x* direction and the phase gradient as being in the *y* direction then the signal, as a function of **k**-space, becomes [19],

$$S\left(k_x, k_y\right) = \int_{-\infty}^{\infty} \int_{-\infty}^{\infty} \rho\left(x, y\right) \exp\left[i2\pi\left(xk_x + yk_y\right)\right] dx\, dy \qquad (1.30)$$

and the volume density function can be calculated using the inverse Fourier transform of $S(k_x,k_y)$, giving

$$\rho\left(x, y\right) = \int_{-\infty}^{\infty} \int_{-\infty}^{\infty} S\left(k_x, k_y\right) \exp\left[-i2\pi\left(xk_x + yk_y\right)\right] dk_x\, dk_y \qquad (1.31).$$

The processing of the signals is done with a computer after acquiring the 2-D signal. Most MRM experiments involve this 2-D Fourier Transform method.

The process of sampling *k*-space to form an image starts with the phase period, when k_x=0 and $k_y \neq 0$. As the experiment progresses in time the spins will evolve in *k*-space along the negative *x* axis. The process can then be reversed to map the signal along the positive *x* axis with k_y= constant. This is known as the read period. The sampling along the *x* axis will then be repeated under a fixed read gradient for discrete increments of k_y. This allows the entire *k*-space to be sampled, and each signal acquisition can be stored as a row in a matrix. G_y is then incremented, which results in the value of k_y being incremented. The

next signal acquisition fills another row in the *k*-space matrix. Repeating this process results in all the rows being filled in for all the columns of the image map.

Image Resolution and Limitations

The signal-to-noise (S/N) ratio is perhaps the greatest limiting factor in MRM experiments. As the size of each volume element is decreased the number of spins contributing to the signal in each voxel will be similarly reduced. Therefore either the experiment duration or the sensitivity of the rf coil must be increased. For a sample of volume $(\Delta x)^3$ the acquisition time for a required S/N ratio will be equal to [19]

$$t = (\rho_o/\sigma_f)^2 a^2 (T_1/T_2)(2.8 \times 10^{-15}/f^{7/2})(1/\Delta x)^6 \qquad (1.32).$$

In this equation (ρ_o/σ_f) is the signal to noise ratio, *a* is the coil radius, and *f* is the spectrometer frequency in MHz. It can be noted from this relationship that if the voxel is halved in all directions but the coil and sample remain the same, the experimental time will increase by six orders of magnitude.

As discussed in the NMR signal detection section signal averaging is one way to increase this ratio, but there are fundamental limitations to this method. Spin relaxation time will limit the repetition rate, and the signal-to-noise ratio will only improve as the square root of the number of experiments. Consider the data taken from a single experiment. If T_1 is equal to 0.5 s then an improvement of an order of magnitude will take an extra minute. Two orders of magnitude will

take an extra hour, and three orders of magnitude will take an extra week. Practically speaking, signal averaging can only be used to improve the data between one and two orders of magnitude.

A high signal-noise-ratio will narrow the intrinsic spectral linewidth of the acquired signal [19]. This determines the resolution limit. It will be narrowest for a molecule with a very high degree of molecular motion, such as a rapidly tumbling water molecule in the liquid state. Crystalline solids, with almost no molecular motion, are nearly impossible to image via standard NMR methods.

Consider a sample of liquid water. The signal acquisition in *k*-space will usually last on the order of a few milliseconds. In this time a single spin will diffuse several microns. This motion will result in a loss of phase coherence and a broadening of the spectral line, limiting the resolution [19]. This diffusive limit to resolution generates a paradox: the intrinsic relaxation linewidth is narrowest for a highly mobile liquid molecule, but a highly mobile liquid molecule will create a new diffusion limitation. Optimization of these two parameters is a great challenge for the NMR scientist. Current methods allow for a resolution of a few microns per pixel, but further refinement of the technology promises to improve the possibilities [19].

Thesis Goal

The goal of this thesis is to explore the various capabilities of magnetic resonance microscopy in regards to the study of proton exchange polymer membranes. Specific areas of observation are molecular mobility as a function of methanol concentration, membrane swelling effects, material inhomogeneity, and diffusion mechanics within the polymer.

MATERIALS AND METHODS

Nafion®-117

All experiments detailed in this thesis were performed on Nafion®-117 proton exchange polymer membranes obtained from the DuPont® Fluoropolymers division. Nafion®-117 was chosen because it is currently the most popular membrane used in PEM fuel cells, and thus has the most relevance to current industrial devices. The dry Nafion®-117 has a thickness of 0.177 mm and an equivalent weight of 1100g [10]. This thickness is significantly greater than the 19.5 μm spatial resolution of the MRM experiments. MRM is therefore able to spatially resolve the interior structures and properties with a reasonable degree of accuracy. There have been previous bulk NMR studies done on Nafion®-117 [6,12,13] which allow a comparison of the observed trends using MRM.

Sample Preparation

The first step in the experimental process was to clean and hydrate the membrane samples according to the procedure of MacMillan *et al.* [13]. A sample approximately 2 cm X 2 cm was cut from the bulk Nafion® sheet. This square was placed in 2M nitric acid (HNO_3) at 80°C for 2 hours. Heating in acid

converted all the ionic sulfate groups in the polymer to their acid form, allowing for the passage of hydrogen protons. The sample was then washed in boiling, nano-pure deionized water to remove any excess acid. Since the manufacturing process is known to impart a number of paramagnetic cations to the sample that can drastically decrease the available NMR signal, the polymer was soaked in 0.01 molar Ethylenediamene tetraacetic acid (EDTA) for 24 hours. EDTA is a chelating agent that will draw out any cation impurities from the sample. After the EDTA soak the sample was once again washed in fresh boiling deionized water, and then placed in 2M HNO_3 for 30 minutes. This second acid wash ensures that any residual cations left on the surface of the polymer will be removed and maximizes the number of acid sites available within the polymer immediately before hydration. After washing in fresh boiling deionized water the sample was placed in the solvent solution to be studied for 24 hours. A 24 hour soak has been found to be adequate for proper hydration of the polymer to occur [13]. The concentrations and volumes of the respective reagents for the solvent solutions used in this study are shown in figure 2.1.

mol fraction MeOH	H_20 (ml)	MeOH (ml)
0	100	0
0.2	14.4	8.1
0.4	10.8	16.2
0.6	7.2	24.3
0.8	3.6	32.4
1	0	100

Figure 2.1 Dilution chart for 24 hour hydration soak

Prior to sample preparation all glassware used in the process was treated to remove cation impurities that could contaminate the samples. The beakers and sample tubes were first soaked in a 50 volume% nitric acid – 50 volume% sulfuric acid mixture for 24 hours. They were then rinsed in boiling deionized water and soaked in 0.01M EDTA for another 24 hours. Following a thorough rinse in fresh boiling deionized water they were allowed to air dry.

Following the 24 hour solvent soak the sample was taken to the MRM lab for analysis. An individual circular sample with a 5 mm diameter was punched out of the 2 cm X 2 cm square. The circular sample was then placed in a Teflon® sample tube with an inside diameter of 5.5 mm. The use of Teflon® for the sample tube is necessary because Teflon® is totally chemically inert and has no protons to give an undesired NMR signal, thus it is invisible to the MRM apparatus. Approximately 0.2 ml of the solvent solution was also added to the sample tube in order to keep the polymer hydrated while experiments were being run. If adequate hydration was not seen in the first sample, a second, third, or fourth sample could be punched from the same prepared square of Nafion®.

MRM Apparatus

For all experiments a Bruker Avance DRX spectrometer was used in conjunction with a 250 MHz superconducting magnet and a Micro5 imaging accessory. The sample container sat in an rf coil of 10 mm internal diameter.

The gradient amplifiers used in the lab were capable of generating gradients up to 2 T/m at 40 A. The computer software used to gather and process the T_2 and diffusion images was a Bruker imaging package named Paravision® 2.1.1. The actual T_2 maps, diffusion maps, and intensity averages were generated using MathWorks Incorporated's MatLab® 6.5.

MRM Experimental Procedure

T_2 Images

The T_2 time for a liquid is very long when compared to the T_2 relaxation time for a solid. This is due to the greater mobility of a liquid molecule as opposed to that of a solid particle held tightly in a lattice [19]. The generation of T_2 images for the type of experiments presented here relies on this fact. The T_2 times for a polymer matrix which contains protons on the polymer backbone will be extremely short due to the restriction of molecular mobility of the polymer membrane itself. The T_2 times for the free liquid in the sample container will be very long, while the relaxation times for the liquid within the membrane will fall in between these two values. This allows the free solvent, the solvent within the membrane, and in theory the membrane itself to be differentiated. Of course for the PTFE based Nafion® used in this work there are no protons on the membrane polymer molecules so they provide no proton NMR signal. The

solvent liquid within the membrane will have restricted mobility due to its absorption by the polymer and its use in forming the rod-like flow channels [6], but it will still be in the liquid form and thus not held rigidly in place.

In order to avoid susceptibility and frequency shift artifacts that would invalidate the data, the phase encoding gradient is applied in the vertical direction while the read gradient is applied in the horizontal direction. The echo time (TE) used for the T_2 experiments was either 17.6 or 6.2 ms. The alternative values were necessitated by lower solvent uptake levels in certain samples. A shorter TE will not change the calculated T_2 relaxation times, but will allow access to more of the NMR signal in the samples with less solvent uptake where the solvent relaxes more rapidly. The recovery time (TR) was 1000 ms for all experiments. Eight averages were used, along with 16 echo images. All T_2 images were generated with matrix dimensions of 64 pixels in the horizontal by 256 pixels in the vertical. The field of view was 0.5 cm by 1.0 cm, resulting in a spatial resolution of 19.5 μm/pixel in the vertical direction and 156.25 μm/pixel in the horizontal direction. In all imaging experiments the phase encode direction is in the vertical direction so as to avoid susceptibility artifacts at the polymer membrane solvent interface [19]. The pulse program used to generate T_2 images is shown in figure 2.2.

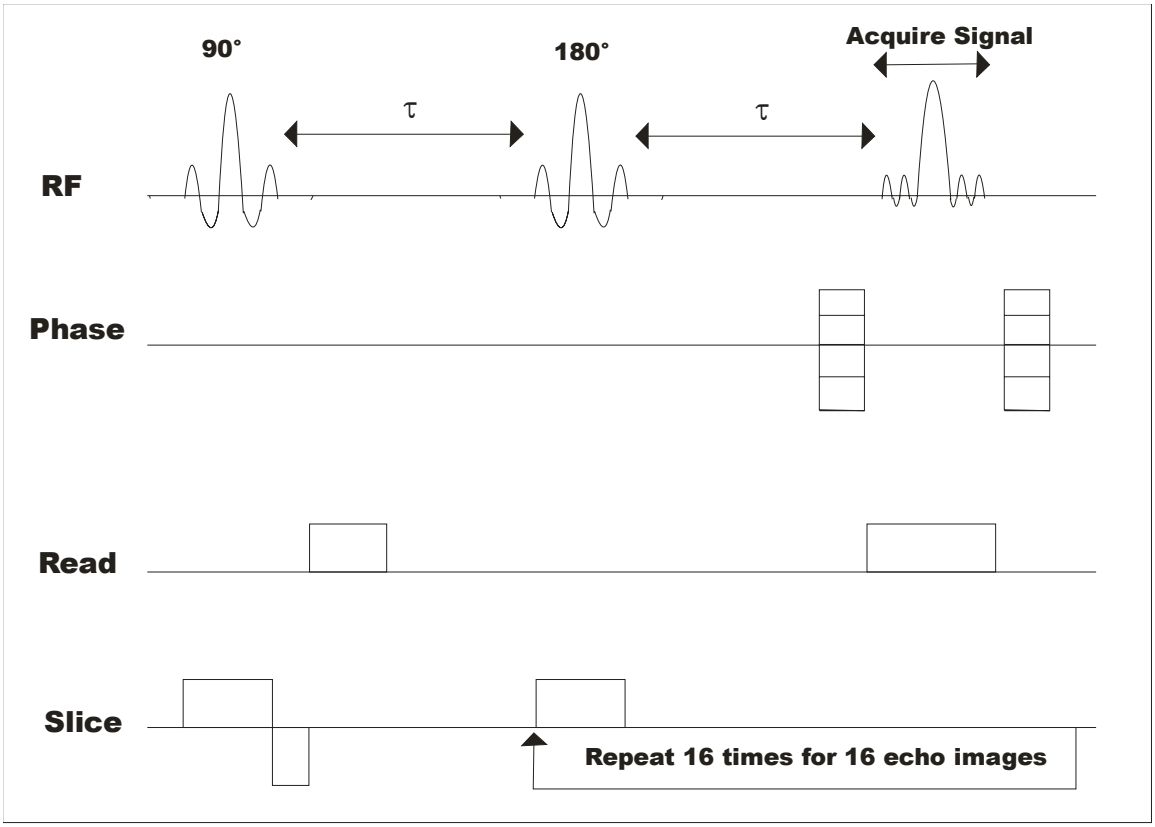


Figure 2.2. Pulse program for T_2 mapping. The RF series is used for both excitation and detection. The phase and read series provides spatial resolution, and the slice series keeps the excitation within the area of interest. The 16 echo images are spaced by the echo time increment (TE = 17.6 or 6.2 milliseconds).

Constructing T_2 Maps

A T_2 map is a single parameter image that is made by calculating a T_2 relaxation time for every individual pixel in the matrix. These values are assigned colors, and the colors are then used to generate the final image. The first step in the calculation process is to fit the signal intensity versus the echo time for each individual pixel. For example, with an echo time of 17.6 ms, the signal intensity for the first image of the first pixel will be acquired at 17.6 ms. The next image

will correspond to a time of 35.2 ms, with each successive echo incremented by TE, for a time equal to N x TE, until all 16 images have been included. The intensity will decrease exponentially according to the equation

$$y = \exp(-TE / T_2) \qquad (2.1).$$

A least squares fit of the data points allows the T_2 value for that pixel to be calculated. The rest of the pixels are calculated in the same manner, until a T_2 value has been determined for every pixel in the matrix. The figure 2.3 gives a graphical representation of the T_2 mapping process for a single pixel.

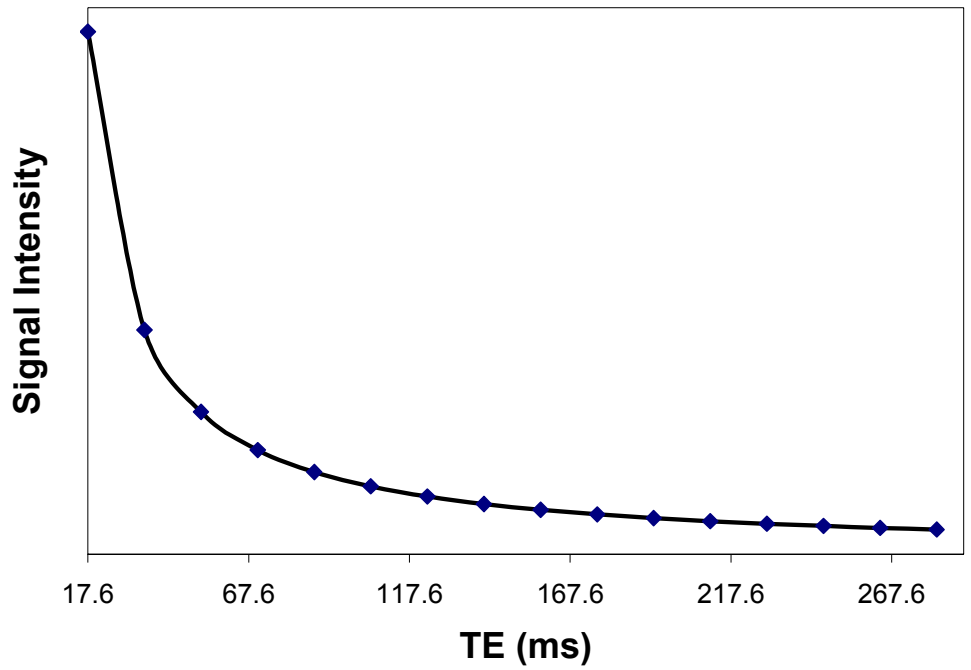


Figure 2.3. Graphical method for calculating T_2 values. Each data point corresponds to a T_2 echo image generated at a TE increment, in this case 17.6 ms. By calculating a least squares fit of the data points the T_2 relaxation time for that particular pixel can be found. Repeating the process for every pixel in the 64 X 256 matrix allows a T_2 map to be generated.

For all T_2 maps the raw data fitting process described above was carried out using the image analysis tool in ParaVision®. Further image analysis, including

generation of the T_2 map images and signal intensity averaging were performed using MatLab®. All scaling factors used in the T_2 mapping process were kept constant in order to allow for direct comparisons between the maps.

Diffusion Images

Diffusion measurements are a specialty of magnetic resonance microscopy. It allows measurements to be made of the rate at which the methanol solution moves through the polymer sample. As can be seen from the pulse sequence in figure 2.4 a diffusion sensitizing gradient pair is applied to the sample in addition to the rf, pulse, read, and slice gradients. At application of the 90° pulse all the spins are evenly aligned in the transverse direction. The first of the diffusion gradients imparts a vector phase angle Φ to the spins proportional to their spatial location. The 180° pulse will reverse the stage of rotation of the spins, and at time Δ the second pulse of the diffusion gradient pair is applied. If the protons are still in their original spatial location then the second diffusion gradient pulse will return the phase angle on each spin to zero. If the protons have moved from their original locations via diffusion, the random motion will result in a randomization of angles that can be measured as an attenuation of signal. This attenuation allows a measurement of how far the protons have moved in time Δ. The process is then repeated with the diffusion gradient pulse pair incremented in strength.

The stronger the gradient the smaller the diffusion distances observable. The signal intensity will be a function of g, Δ, and δ, and the mathematical expression for the measured signal is

$$E = \exp(-\gamma^2\delta^2g^2D\Delta) \qquad (2.2).$$

In these equations E is the signal intensity, γ is the gyromagnetic ratio, δ is the pulse duration, g is the gradient strength, D is the diffusion coefficient, and Δ is the time increment between the first and second diffusion gradient pulses. Since a large diffusion gradient pulse will access shorter displacement distances, there is a fundamental hardware limitation to the minimum D value that can be measured, according to the maximum gradient strength that can be generated.

For all experiments the following parameters were used: the matrix was 64 pixels horizontal by 256 pixels vertical, the repetition time was 0.5 seconds, the echo time (TE) was 20.3 ms, Δ was 12 ms, 8 diffusion gradients were applied (100 mT/m, 300 mT/m…..1500 mT/m), 8 averages were used, and the recovery time (TR) was equal to 500 ms.

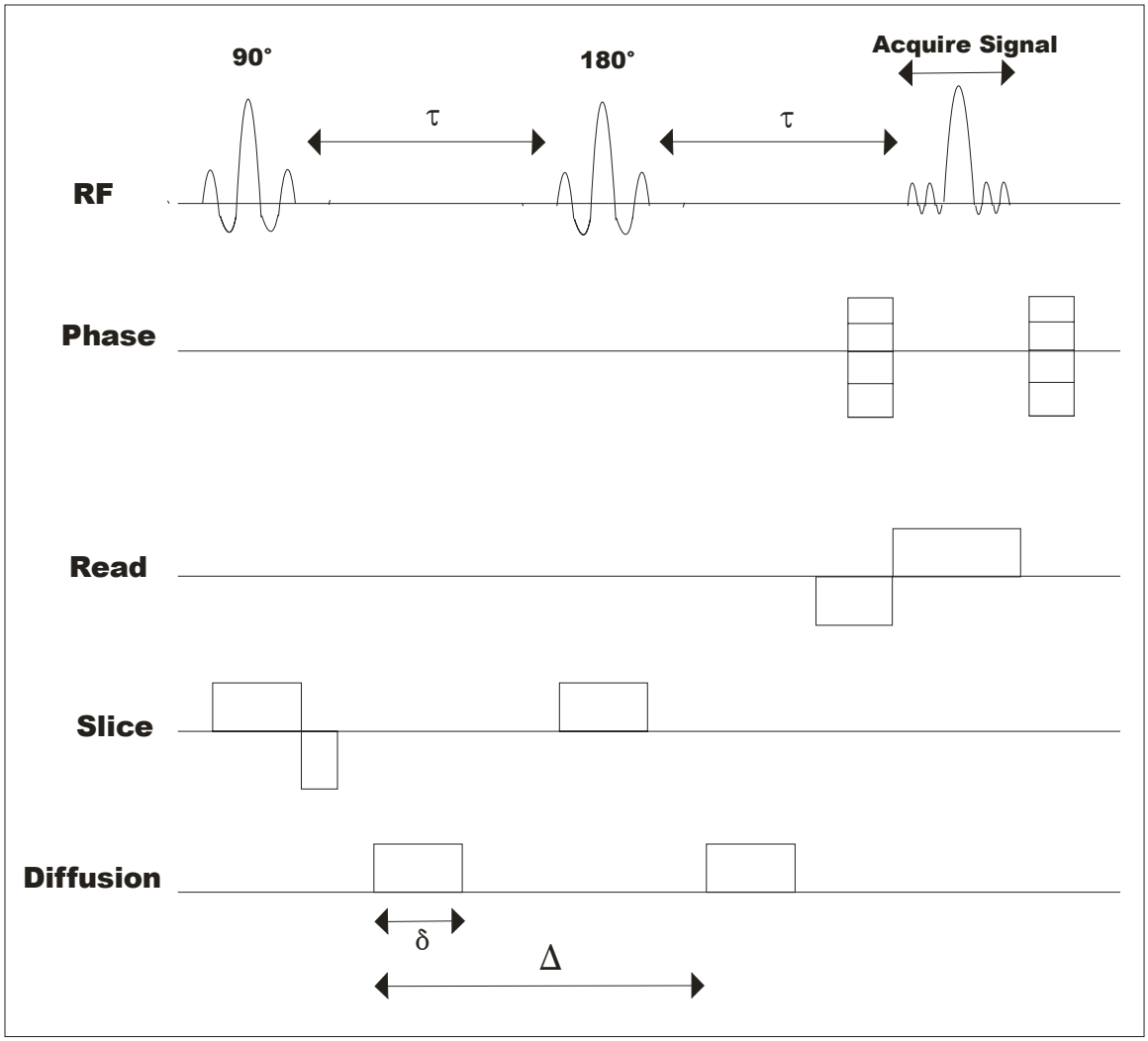


Figure 2.4. Pulse program for diffusion mapping. The diffusion gradient pulse pair imparts a vector phase angle Φ to the spins. When the spins are reversed and come back to their original locations the residual angles will tell how far the protons have moved in time Δ, and randomization of phase angles due to random diffusive motion attenuates signal.

Constructing Diffusion Maps

All diffusion data were processed using MatLab®. First a graph of the natural log of signal intensity versus the gradient increment was generated for the 8 diffusion points in each pixel. This is known as a Stejskal-Tanner plot [19].

An example is shown in figure 2.5. A linear regression line was fitted to the data points, and the slope is equal to the diffusion coefficient. Using this method, however, results in uneven weighting of the later images if data points near the end of the experiment are below the signal to noise ratio, and are thus unreliable. A regression line will be skewed to give the best possible fit to all the data points, and consequently only the first five images were used to make the final diffusion maps. A color was assigned to each diffusion coefficient calculated, and the values were mapped for every pixel in the matrix. Masking, another name for setting all intensities below a specified threshold value equal to zero, was employed in order to avoid noise outside of the sample container. The scaling factors used for each diffusion map were kept constant so direct comparison between the maps is possible.

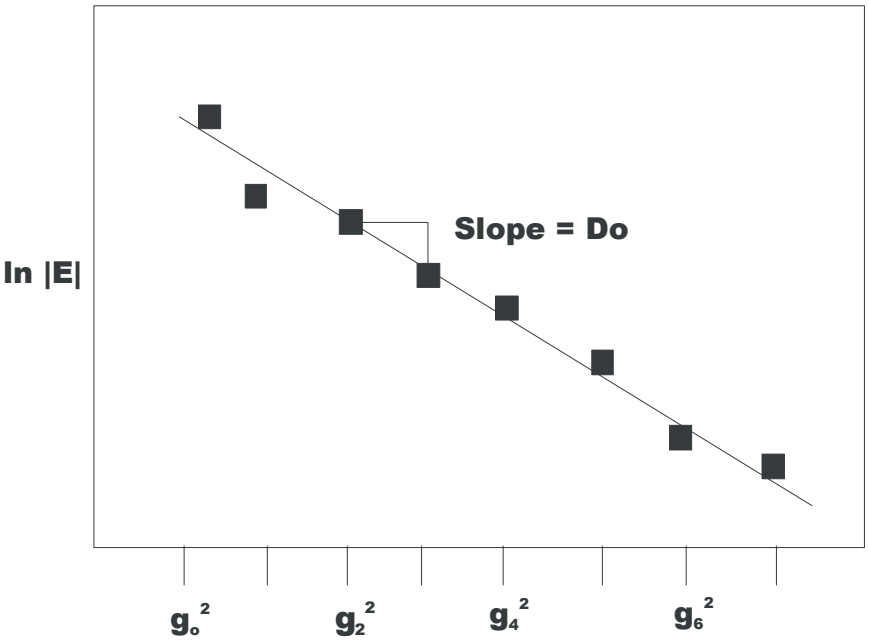


Figure 2.5. Sample Stejskal-Tanner plot of diffusion data. The natural log of the signal intensity is graphed versus the square of the gradient strength, and the slope of the regression line is equal to the diffusion coefficient D_o.

Membrane Heterogeneity Experimental Scheme

Membrane Sampling Procedure

In order to test the material homogeneity of Nafion®-117, a single 3 cm by 3 cm square was prepared according to the sample preparation procedure discussed previously. The membrane was soaked in 0.2 mol fraction methanol for 24 hours. The sample sheet was notched at the top and on the right side in order to maintain the proper face-up orientation of all samples. Individual samples were punched from the membrane according to the diagram shown in figure 2.6.

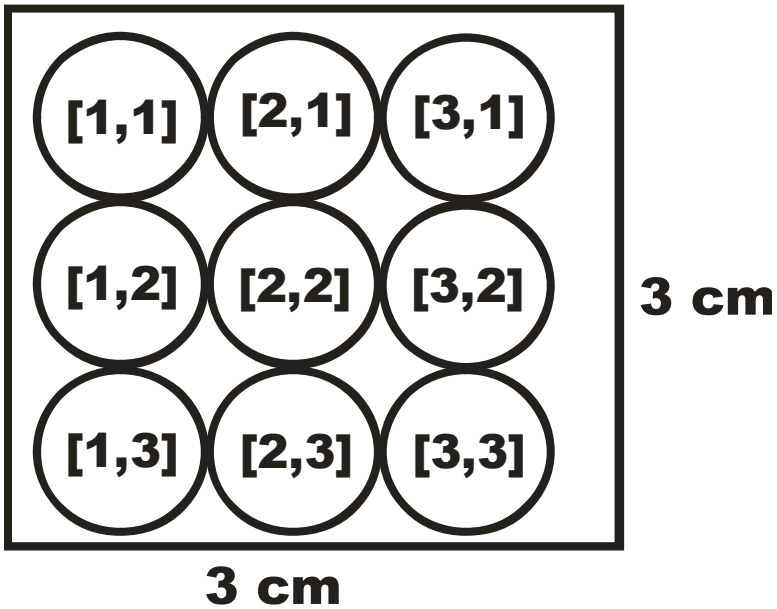


Figure 2.6. Punch scheme for material inhomogeneity experiment. Number designations correspond to standard matrix notation. Longitudinal direction is from top to bottom while transverse direction is from left to right. All samples were notched at the top (0°) and double notched at the right side (90°) to maintain orientation during the experiment.

Special care was taken during the punch process to maintain the sample orientation in relation to the square. Each sample was notched once at the top and twice at the right side, 90° clockwise from the first notch. The samples were punched immediately prior to their placement in the MRM apparatus, and the sample square was kept in solution while the experiments were being run. All samples were placed face-up in the sample tube.

Experimental Setup

The first experiment run on each sample was a T_2 map in the longitudinal direction. In order to accomplish this the orientation of the membrane within the MRM apparatus had to be determined. A very fast image was generated in order to ensure that the sample was lying flat and centered in the coil. Next an image was made looking straight up at the polymer. This image allowed the notches to be clearly seen. By going into the slice selection tool in ParaVision® the excitation slice for the T_2 map could be specified as running through the first notch and the center of the sample. A T_2 imaging experiment was then run with the following parameters: the matrix was 64 pixels horizontal in the read out direction by 256 pixels vertical in the phase encode direction. The field of view was 1.0 X 0.5 cm, TR was equal to 1000 ms, TE was equal to 6.2 ms, 4 averages were used, and 16 echo images were generated.

The next step was to take T_2 data in the transverse direction. This was simply done by rotating the excitation slice 90° in the ParaVision® slice selection tool so it sat in between the two notches on the right side of the polymer. Once the slice orientation had been changed, the T_2 imaging procedure used for the longitudinal study was repeated with the exact same parameters. Once T_2 images had been generated in both directions the sample was removed and stored in a separate sample container filled with 0.2 mol fraction methanol solution. A new sample was punched according to the punch scheme, and the process was repeated. After all nine samples had been run the experiments on the first sample were repeated in order to determine if an extra 12 hours spent in solution would alter the hydration levels observed in the first experiment. All data was then processed and T_2 maps generated according to the calculation scheme outlined in the Constructing T_2 Maps section above.

RESULTS AND DISCUSSION

Solvent Mobility as a Function of Methanol Concentration

T_2 Measurements

In the materials and methods section it was explained how measuring the T_2 relaxation time of a sample gives quantitative data about how much solvent the polymer has absorbed. Better solvent absorption leads to more liquid within the sample, which in turn leads to longer T_2 times measured within the polymer. However, these longer T_2 times are not purely due to solvent uptake. As the membrane swells it allows for more solvent to be adsorbed into the polymer. But at the same time the size of the flow channels discussed in the introduction will also be increasing. This allows the overall mobility of the solvent within each sample to increase. In other words, the liquid inside the sample will behave more like a free liquid since it is not interacting with the channel walls as strongly. T_2 times will also increase as the density of the polymer decreases due to swelling. The mass of the polymer remains constant, but as the membrane swells there will be less of this mass in a given volume. The simplest method for observing the data is to take a T_2 map of a sample at each methanol concentration and place these maps side by side. This has been done in figure 3.1.

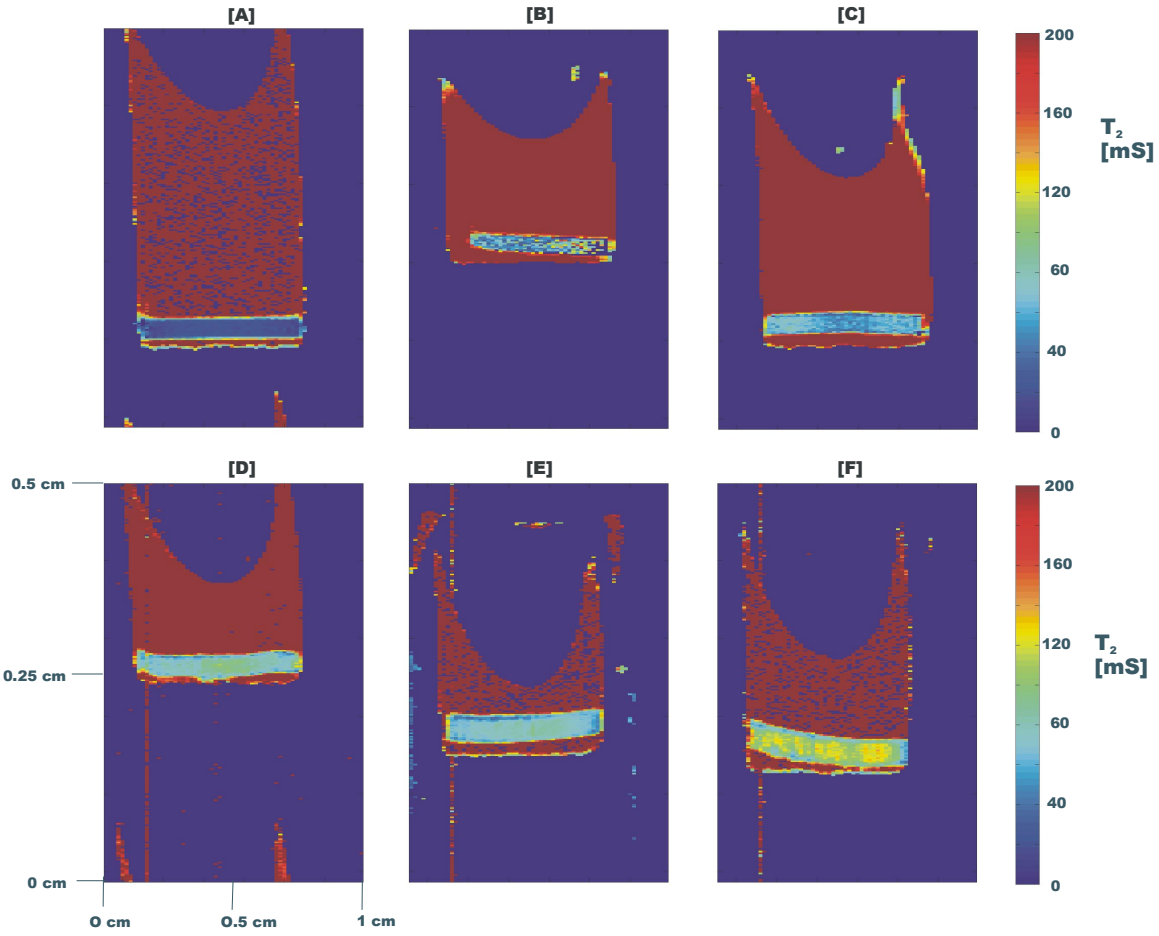


Figure 3.1. T_2 maps for the various methanol concentrations. A, B, C, D, E, and F correspond to 0, 0.2, 0.4, 0.6, 0.8, and 1.0 mol fraction methanol, respectively. As the concentration increases the amount of free solution within the polymer also increases, as can be seen by the transition from dark blue in the pure water sample to yellow in the pure methanol sample. Membrane swelling can also be observed to increase with increasing methanol. Material inhomogeneity can be most clearly seen in samples B and C.

Figure 3.1.A shows a polymer that was prepared in a solvent consisting of pure water. As can be seen from the dark blue color within the sample and in the color bar a very low T_2 relaxation time was observed. Figure 3.1.B, the 0.2 mol fraction methanol sample, shows a longer T_2, but it also shows inhomogeneous

relaxation times across the sample. The flecks of color distributed randomly across the polymer show how some areas will have excellent solvent mobility, others moderate mobility, and in places there will be almost no mobility at all. Figure 3.1.C shows a sample prepared in 0.4 mol fraction methanol. This sample still shows some minor variations in the center of the disc, but overall the solvent mobility level is higher than the first two samples. The 0.6 mol fraction methanol sample in figure 3.1.D shows a light blue color with some areas fading into greenish-yellow. As the color bar indicates, this corresponds to longer T_2 times caused by increasing solvent mobility and membrane swelling. Figure 3.1.E, the 0.8 mol fraction methanol sample, shows almost the same mobility as the 0.6 sample. The difference is along the edges, where the T_2 values are extremely short. This corresponds to areas of the polymer with very little solvent absorbed and a lesser degree of swelling compared to the rest of the sample. Considering the overall similarities to the 0.6 sample, material inhomogeneities, as discussed later, were likely the cause of the similarity. Figure 3.1.F shows a sample soaked for 24 hours in pure methanol. This image shows the greatest solvent mobility of all the samples, with many areas bright yellow in color, consistent with the soluble nature of Nafion® in methanol. These areas, however, are intermixed with light green and even light blue, showing that even when a sample is swollen the molecular mobility levels are not constant across the polymer. The overall series shows how the use of methanol solutions in the

sample preparation process results in samples with greater levels of solvent mobility according to the strength of the methanol solution used.

While the above method is simple and easy, it does not give any quantitative data about the samples. In order to develop numbers, the actual T_2 values need to be analyzed as a function of the location within the sample container. This has been done in figure 3.2.

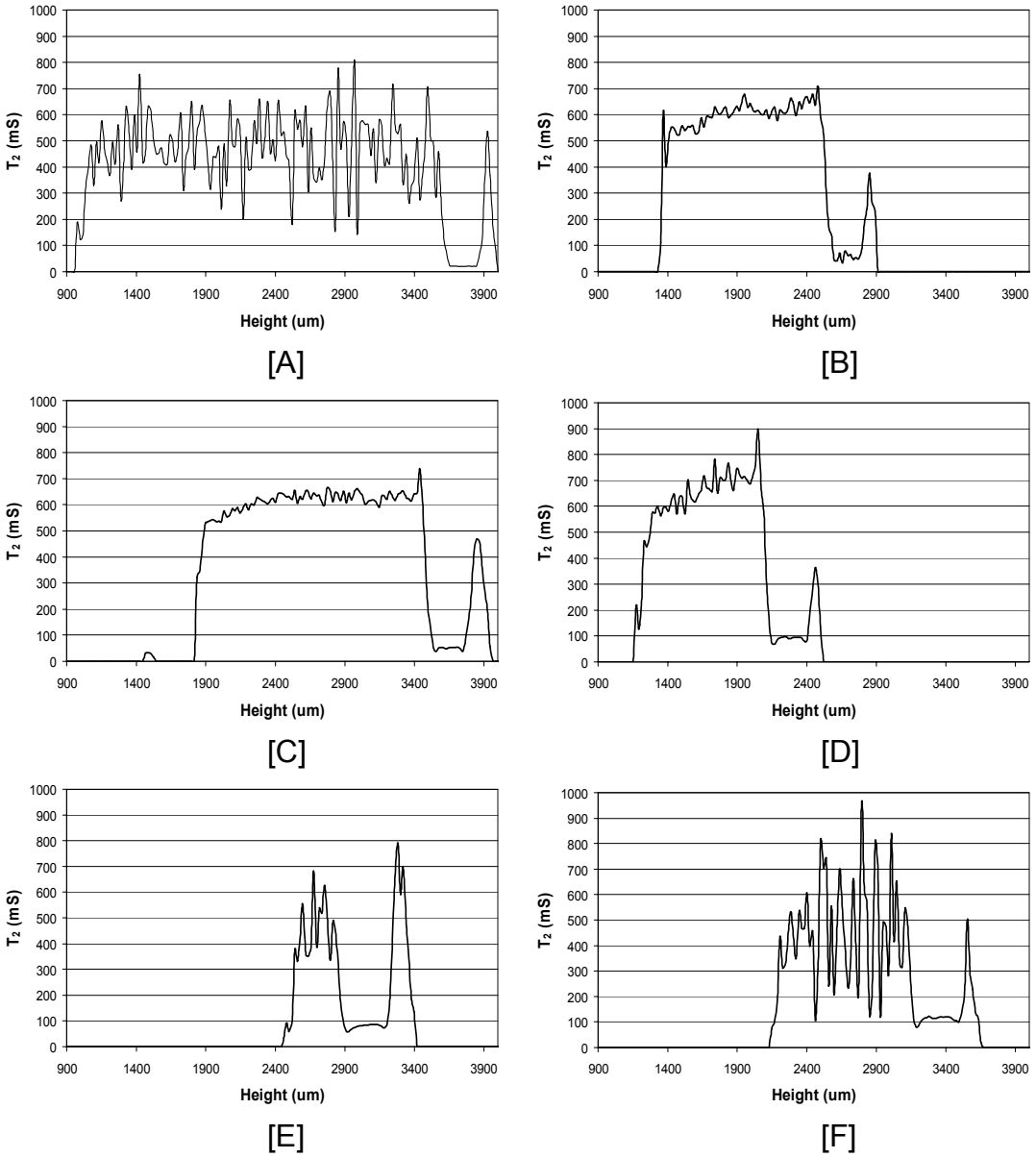


Figure 3.2. Graphs showing the average T_2 values in milliseconds within a 5 pixel horizontal region of the sample as a function of the sample container height in microns. A, B, C, D, E, and F correspond to 0, 0.2, 0.4, 0.6, 0.8, and 1.0 mol fraction methanol, respectively. The high T_2 values of the free solution can be seen on the left side of each graph. The sudden dip and relatively constant lower values correspond to the restricted motion of the particles within the polymer, followed by a spike as the solution beneath the membrane is sampled. The shorter echo time (6.2 ms) used in A, E, and F results in increased noise within the free liquid.

The intensity graphs shown in figure 3.2 were made by averaging the T_2 values (shown in the T_2 map image) vs. height for a 5 pixel (781.25 μm) horizontal band of the image. The free liquid, with a long T_2 relaxation time, will give a very strong signal. The liquid within the polymer, however, relaxes an order of magnitude faster, and this behavior can be read directly from the intensity graphs. In all cases the T_2 value sharply goes from zero outside of the sample container to several hundred milliseconds for the free liquid. There is significant noise within the free liquid region, especially in those samples using a TE of 6.2 ms (samples A, E and F), since the experimental time range covered, N x TE, is not adequate to calculate the longer T_2's of the free solvent.

Although it is not immediately apparent that A, E, and F have been smoothed, without the averaging process the attempt to fit the long relaxation time data with such a short echo time results in spikes in the observed T_2 of the free liquid from zero milliseconds to several tens of seconds. The averaging process cannot remove all the noise, but it can keep it within a range that allows the area of interest to be observed.

The next sharp change is seen at the edge of the polymer, corresponding to the sudden drop in intensity levels to below 100 ms. At this boundary the sudden change in T_2 times provides a sharply defined border between polymer and liquid, allowing swelling effects to be measured within the limits of the spatial resolution. The T_2 values within the membrane are relatively constant, due to the averaging method employed and the scaling of the graphs. The sharp increase

in the T_2 values corresponds to the bottom membrane boundary, and the small amount of liquid beneath the polymer is then sampled.

These graphs show how the average T_2 relaxation time for the liquid within the polymer increases as the methanol concentration increases. The T_2 values within the membrane for the pure water sample, graph A, are extremely low at 21.2 ms. B with T_2 times equal to 35.1 ms, C with T_2's equal to 51.5 ms, and D with T_2's equal to 92.1 ms all show an increase. There is a dip at 0.8 mol fraction methanol, the E sample, with T_2 relaxation times of 82.1 ms, but material inhomogeneities, discussed in detail later, can impact measured average T_2 values at a fixed methanol concentration as shown in figure 3.4. Since the pure methanol sample shows agreement with the general trend and an average T_2 of 118.3 ms, the data point aberration at 0.8 mol fraction methanol is likely due to sample heterogeneity. These longer T_2 times show how at increased methanol concentrations the membrane swelling and molecular mobility both increase.

The numbers used to generate the T_2 average graphs were also used to develop quantitative values for the T_2 times in the liquid, T_2 times within the polymer, and membrane swelling. The average T_2 times within the free liquid, for example, are graphed in figure 3.3.

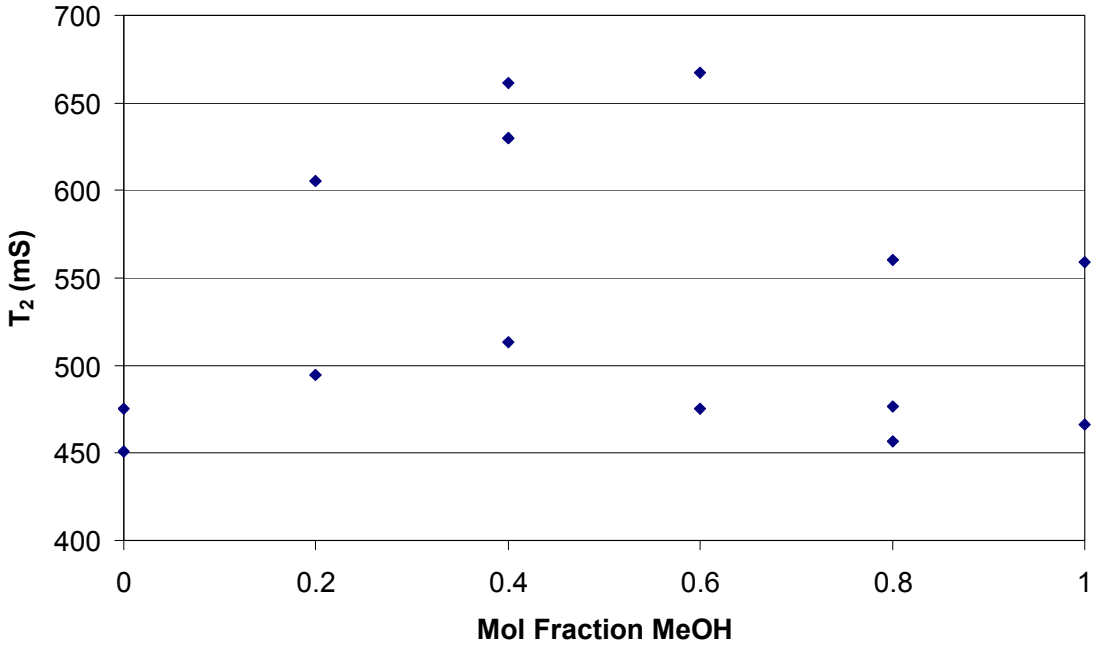


Figure 3.3. Graph of the average T_2 values of the free liquid as a function of concentration for a small slice of the sample. Averages over 5 horizontal pixels are used to smooth out noise within the data. Due to the faster relaxation times within the polymers a shorter echo time was used in the experiments. In order to generate a smooth fit to the liquid data a longer echo time would be necessary.

Figure 3.3 shows the importance of choosing the proper T_2 parameters. Since the experiments were intended to give data about the liquid within the polymer rather than the solution outside of it, there is significant scatter within the data due to the short TE time increment and the number of spin echoes acquired. In order to make a more accurate measurement of the free liquid T_2 the echo time would need to be increased.

The average T_2 within the polymer itself is of primary interest. The

numbers in graphical form for multiple membrane samples at each methanol mol fraction are shown in figure 3.4.

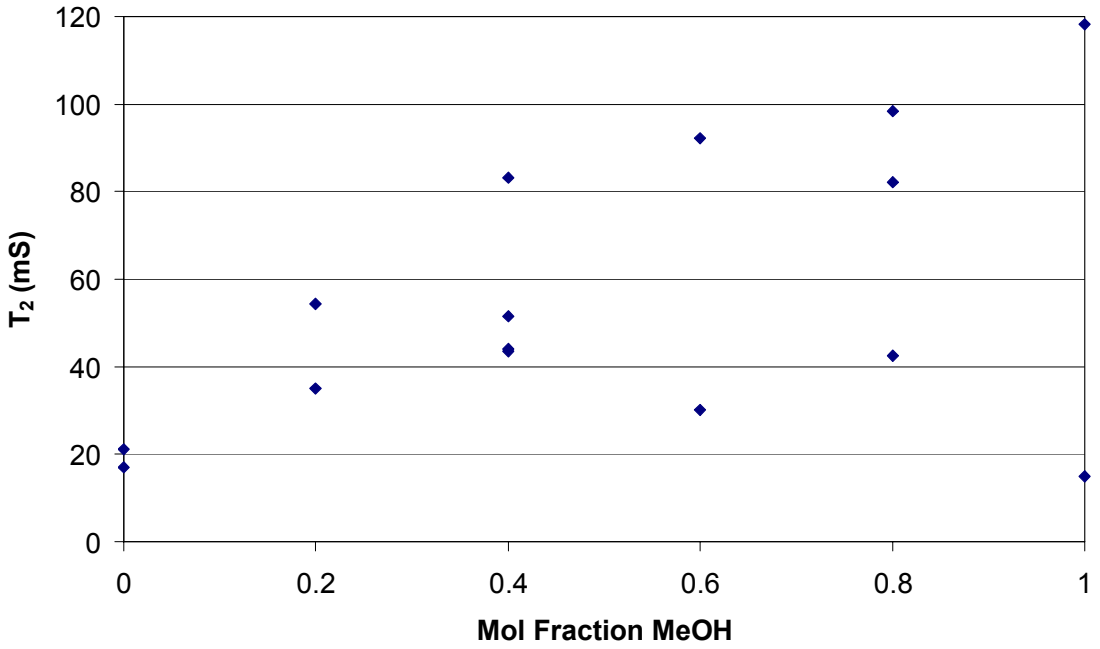


Figure 3.4. Graph of the average T_2 values within the membrane as a function of concentration for a small slice of the sample. The material inconsistencies, as outlined in the material inhomogenity section, can account for the extremely scattered data points. Samples at the same concentration with different solvent mobility levels can show great variety in the T_2 values measured.

There is significant scatter in this data as well, although this is not due to the experimental parameters. The general trend seems to be that the T_2 values are increasing as the methanol mol fraction increases, but it is obviously not a hard and fast rule, and quantification of the data is difficult. The fits to the exponential decay of the image intensities are good, so the simplest explanation is that due to material inhomogeneities solvent mobility within the polymer is extremely

variable. This will be true regardless of the methanol concentration used in the preparation procedure, and is born out by data discussed below.

To calculate the membrane swelling T_2 amplitude values are used to highlight the boundaries between the polymer and free liquid. Since the interface is such a sharp spike on the intensity graph, calculating a half-height value is extremely simple. These half-height values are taken to correspond to the edges of the polymer, and by taking the difference the membrane thickness can be calculated. The final thicknesses are given in figure 3.5.

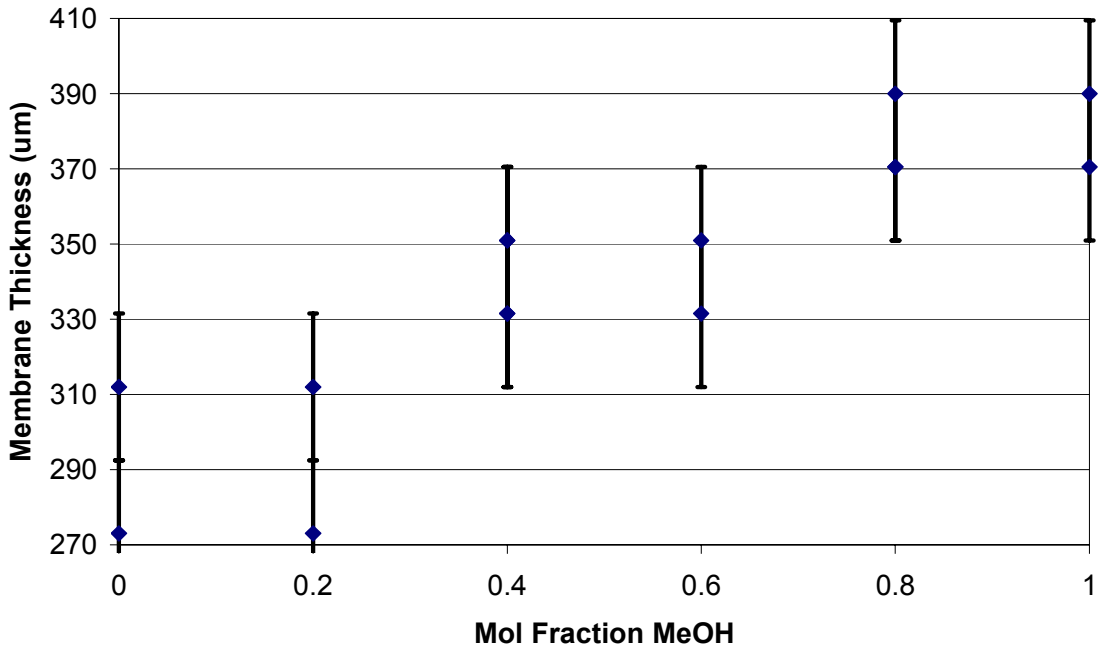


Figure 3.5. Graph showing the membrane swelling as a function of methanol concentrations. As the mol fraction of methanol increases the degree of swelling demonstrated by the polymer also increases. Error bars correspond to spatial resolution of 19.5 μm.

Figure 3.5 shows how as the concentration of methanol increases, the solvent mobility within the polymer will also increase. This can be observed by

the increased swelling of the membranes. The dry Nafion®-117 has a thickness of 177μm. The change in the volume of the membrane as it swells will be given by the equation

$$\Delta V = \pi R^2(h_{sol} - h_{dry}) \qquad (3.1).$$

Here R is the radius of the polymer disk, h_{sol} is the thickness of the prepared membrane, and h_{dry} is the thickness of the dry membrane. Since the membranes are punched after 24 hours soaking in the solvent solution, any subsequent changes in R will be negligible, and the swelling can be measured in a single direction. As mentioned in the introduction, the polymer will continue swelling as it continues to absorb solvent. The degree to which the polymer swells, however, will be within the spatial resolution of the MRM for small differences of the volume fraction of solvent within the polymer. This accounts for the observed pairing of the data points. While the membrane does hydrate better and thus does swell more at 0.2 mol fraction methanol as compared to pure water, the difference in swelling is not pronounced enough to be spatially resolved in the MRM experiments. Thus the data points are exactly the same. The difference between pure water and 0.4 mol fraction methanol, however, is definitely within the MRM's ability to discern. Consequently there is an observed increase in membrane thickness as the mol fraction methanol is increased.

Diffusion Measurements

To visualize the swelling and spatial distribution of molecular translational motion, diffusion as a function of methanol concentration is spatially resolved in diffusion maps. Using the same scaling factors and placing diffusion maps side by side has been done in figure 3.6 for a representative sample at each concentration.

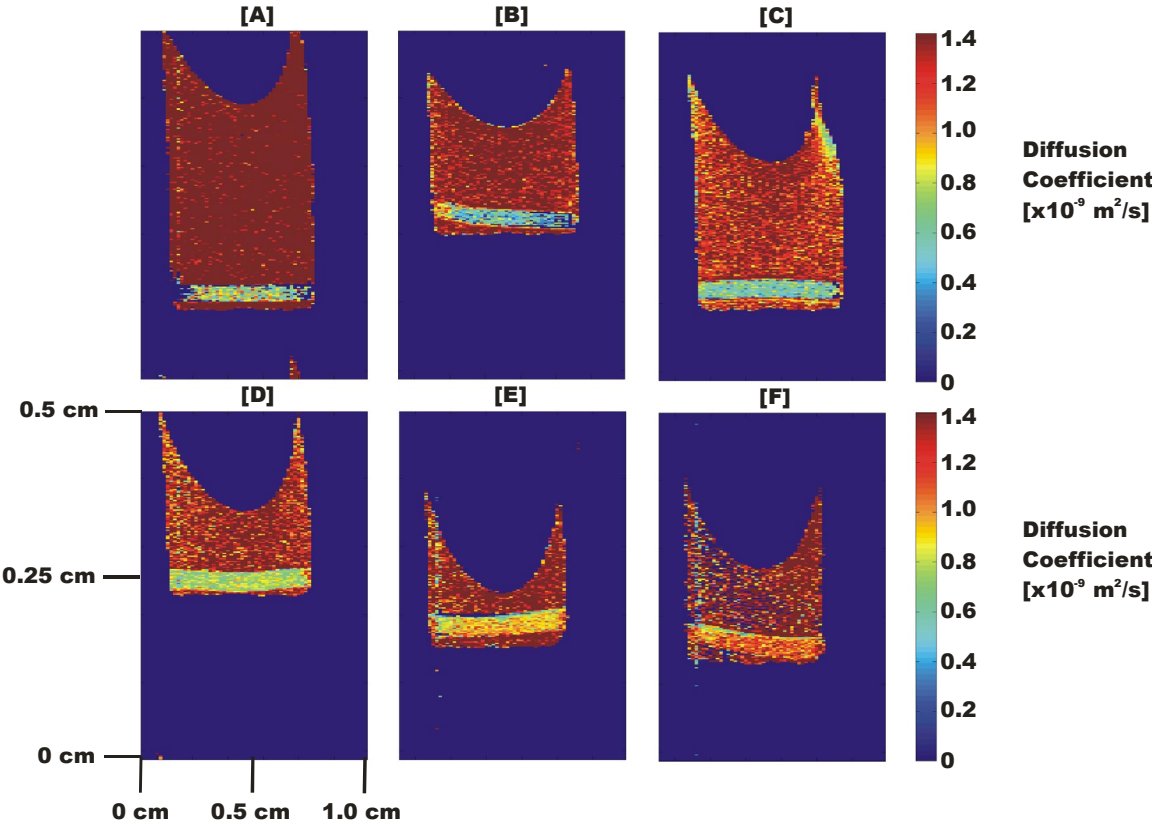


Figure 3.6. Diffusion maps for the various methanol concentrations. A, B, C, D, E, and F correspond to 0, 0.2, 0.4, 0.6, 0.8, and 1.0 mol fraction methanol, respectively. As can be seen the diffusivity starts out as slightly higher within the polymer, dips slightly at 0.2 mol fraction, and then increases steadily as the methanol concentration increases.

Figure 3.6.A shows the diffusivity of pure water within the sample. Diffusion coefficients drop to a minimum at 0.2, and then increase steadily as the concentration increases. The minimum at 0.2 is due to both lower solvent uptake levels in the polymer as seen in the T_2 study and a decrease in the diffusion coefficients of both the water and the methanol OH protons. The molecular level structure of the free solvent methanol solutions will decrease the diffusion coefficient of the two proton groups in the free solvent when compared to pure water and pure methanol [9], but the difference in diffusion coefficients between the two groups is only significant at very low methanol concentrations [25]. This behavior is overcome as both solvent levels and diffusion coefficients of the protons increases with methanol concentration.

The intensity averages were generated in the same fashion as those for the T_2 measurements, namely by averaging over a 5 pixel (781.25 μm) horizontal section of the image. The graphs are shown in figure 3.7.

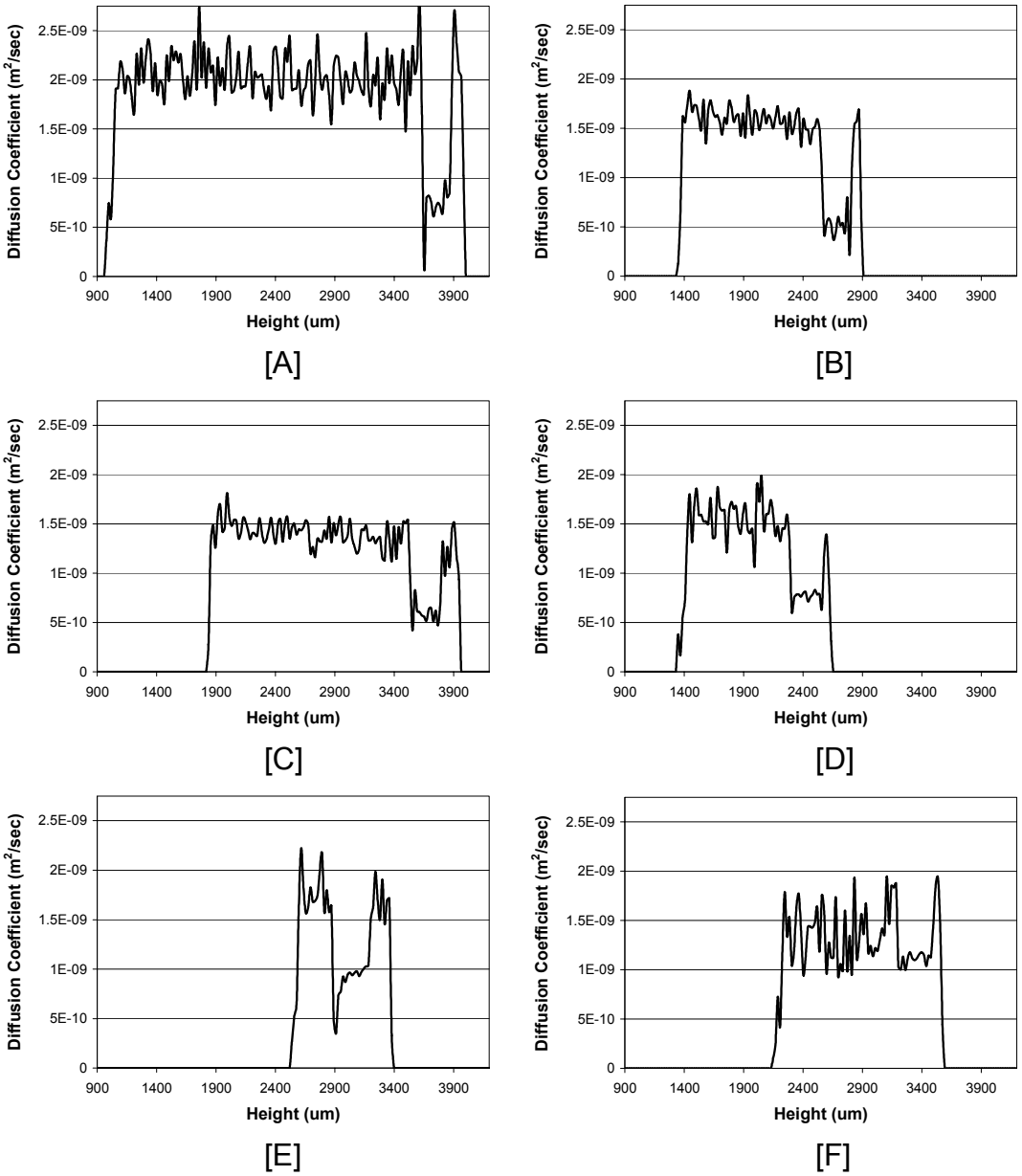


Figure 3.7. Graphs showing the average diffusion coefficient values in m^2/sec within a 5 horizontal pixel section of the sample as a function of the sample container height in microns. A, B, C, D, E, and F correspond to 0, 0.2, 0.4, 0.6, 0.8, and 1.0 mol fraction methanol, respectively. The high diffusion values of the free solution can be seen on the left side of each graph. The sudden dip and relatively constant lower values correspond to the restricted diffusion within the polymer, followed by a spike as the solution beneath the membrane is sampled. The evolution of the average diffusion coefficient within the membrane as a function of concentration closely mimics that seen by Hietala *et al*. [9]

In these graphs the fast molecular motion of the free liquid results in high values of the diffusion coefficient in the liquid and a low diffusion coefficient for the liquid within the sample. These high values and low values therefore give the same general behavior as the T_2 intensity graphs. The intensity will be zero outside of the sample container, there will be a sharp spike as the free liquid is sampled, a sudden decrease as the boundary between the polymer and liquid is crossed, relatively constant diffusion within the sample, a spike as the lower boundary is then crossed, and then a sampling of the liquid below the polymer. In this case the noise in the free liquid is produced by the large diffusion gradient values applied, optimized to fit the much slower diffusion within the polymer membrane.

The numbers used in the generation of the intensity averages were then graphed for comparison with accepted diffusion values for methanol and bulk Nafion® studies. The behavior of the free liquid is shown in figure 3.8. The trends observed in these experiments correlate well with previous NMR experimental values for free diffusion of water and methanol solutions [9, 26]. The data points for the free diffusion of pure methanol show the greatest error. This is due to the experimental parameters being designed to measure diffusion within the polymer rather than the free liquid. Accurately measuring the self-diffusion coefficient of pure methanol would necessitate a smaller diffusion gradient value to handle the larger diffusion coefficients.

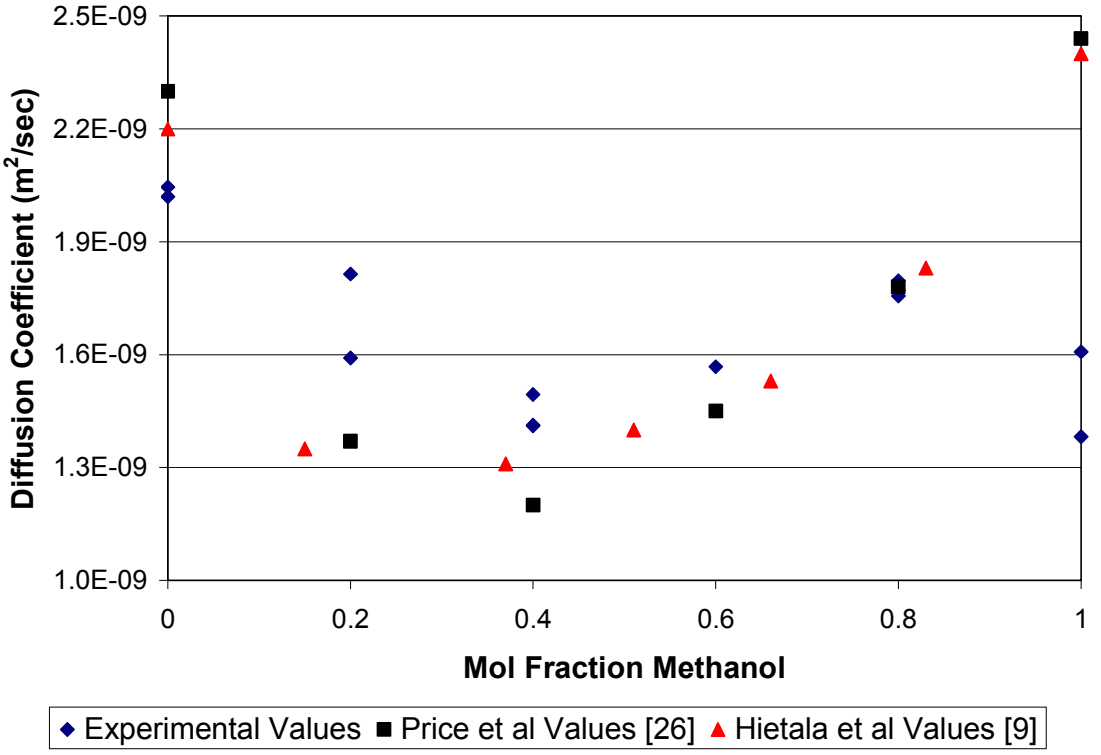


Figure 3.8. Graph of the average self-diffusion coefficient within the free liquid versus the concentration of the solution. The numbers generated show excellent agreement with the values presented in Price *et al.* [26], and Hietala *et al.* [9], with the exception of the pure methanol data points. In order to fit the faster diffusion coefficient of the methanol, a significantly smaller diffusion gradient value is required. The experiments are optimized to study the solvent within the membrane, not the free solvent, so these data are qualitative in nature.

The diffusion coefficients within the polymer itself show excellent agreement with the trends and values outlined in the Hietala *et al.* paper [9]. The diffusion coefficient for samples in pure water starts out at a relatively high value. It decreases to a minimum in the 0.2 to 0.4 range, and then increases linearly. The decrease and linear increase are approximately equal in scale to those seen in the Hietala *et al.* paper [9], in which bulk NMR measured diffusion over much larger membrane samples than used in this work. The experimental diffusion

coefficients generated in this study and the values observed by Hietala *et al.* are shown in figure 3.9. The variations between the Hietala *et al.* [9] data and this work is most likely due to the heterogeneity of the PEM's. The spatially resolved data includes spatial variations in the PEM while in the larger PEM samples of Hietala *et al.* [9] the spatial heterogeneity is averaged out.

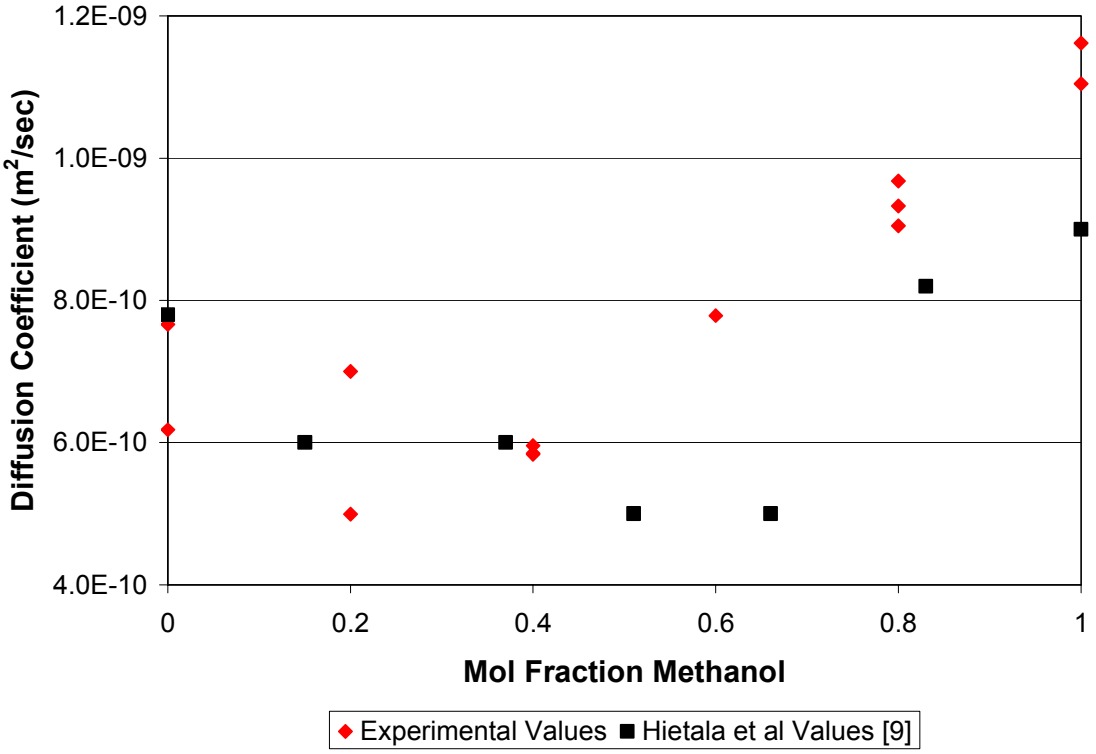


Figure 3.9. Diffusion coefficients within the polymer as a function of methanol mol fractions for multiple experimental runs. The data shows extremely close agreement with the general trends and values outlined in Hietala *et al.* [9], namely that diffusion coefficients start out at a rather high value for pure water, decrease to a minimum around 0.5 mol fraction methanol, and then steadily increase to a level above that of the pure water.

Diffusion maps can also be used as a gauge of membrane swelling. Because the diffusion intensity graphs have the same sharp spike when

encountering the boundary between the liquid and the polymer, a half-height value can be read off the graphs in the same manner as those in the T_2 measurements. In both cases the MRM signal is simply used for contrast. Figure 3.10 shows the quantitative measurement of the membrane swelling as measured by diffusion.

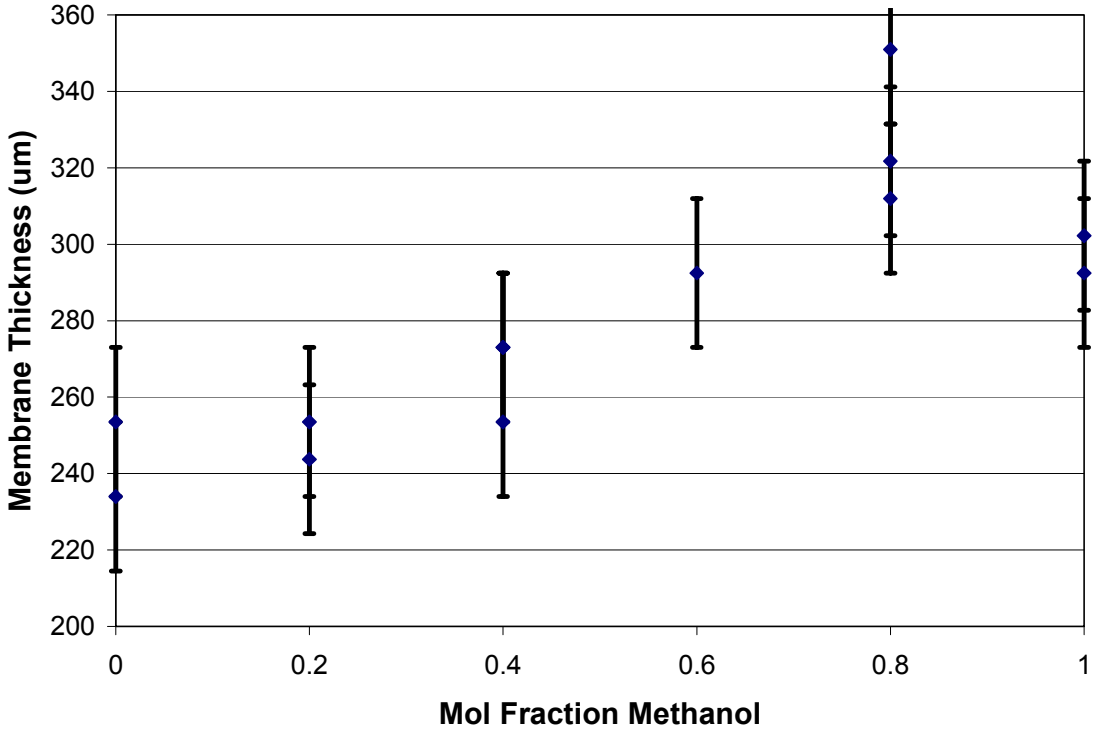


Figure 3.10. Graph showing the membrane swelling as a function of concentration for multiple diffusion experiments. As the amount of methanol in the solution increases the membrane swells to a greater degree. Error bars correspond to the spatial resolution of 19.5 μm. This data agrees nicely with the trends seen in the swelling experiments using T_2 measurements as outlined in figure 3.5.

As figure 3.10 clearly shows the membrane swells to a greater degree in increasing methanol concentrations. While the numbers themselves are not in perfect agreement with those found using T_2 methods, the general trends of the

data are consistent. The thicknesses of the membranes measured via diffusion are consistently smaller than those measured using the T_2 values. Figure 3.11 gives an average difference for the swelling effects as measured by the two different methods.

Mol Fraction Methanol	Total Width via T_2 (microns)	Total Width via Diffusion (microns)	Difference (microns)
0	312	253.5	58.5
0.2	273	253.5	19.5
0.4	331.5	253.5	78
0.6	331.5	292.5	39
0.8	390	321.75	68.25
1	390	302.25	87.75

Figure 3.11. Differences in the quantitative measurement of membrane swelling via T_2 and diffusion mapping. Measurements taken from the T_2 maps are consistently higher than those made by diffusion mapping.

The difference in values between the two methods is due to the differing molecular level effects being measured by the MRM experiments. The contrast used to measure swelling by diffusion mapping is dependent upon the translational motion of the molecules within the polymer. A sharp difference between the free liquid and the liquid within the polymer will not be observed until the diffusive motion of the particles is restricted by the flow channels present within the membrane. Swelling effects measured via T_2 mapping, on the other hand, are dependent upon both translational and rotational motion of the molecules. This means that there will be significant molecular interactions

between the liquid and the polymer at the membrane/liquid interface. Consequently the T_2 method will measure a boundary layer of restricted solvent at the polymer edges that is invisible in the diffusion maps. The measurement of these restricted solvent boundary layer's rotational motion results in a higher value for the membrane thickness.

Material Inhomogeneity

If a perfectly homogenous sample of Nafion®-117 were prepared as a single unit, the T_2 values across the membrane would be equal and constant everywhere. Any sample taken from this unit would show the exact same T_2 values, and there would be no deviation at any point. A T_2 map would show a single band of color, and the color would be exactly the same no matter where the sample was taken. This is not the case observed. At the beginning of the PEM study the prepared Nafion® samples demonstrated extremely variable molecular mobility from sample to sample. All systematic errors in the preparation procedure were identified and eliminated, but the variations persisted. Some samples would show short T_2 relaxation times within the membrane, while other samples prepared in exactly the same manner would show long T_2 times. An example of this signal disparity is shown in figure 3.12.

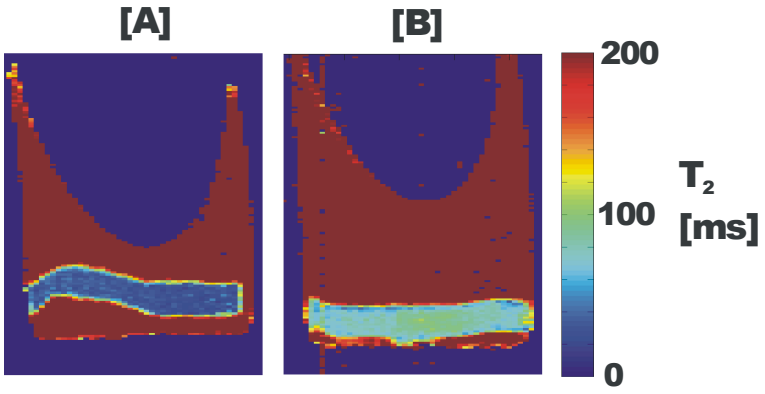


Figure 3.12. T_2 maps for two samples prepared separately in 0.6 mol fraction methanol. Sample A shows average T_2 values of 30 ms, while sample B shows average T_2 values equal to 90 ms. Both samples were prepared from the same sheet of Nafion®-117 according to the sample preparation procedure outlined in the materials and methods section.

In order to determine if this was a material issue that could not be affected by preparation methods, the inhomogeneity experiment described in the Materials and Methods section was designed. The first experiment generated a T_2 map in the longitudinal direction for membrane samples cut from a 3 cm by 3 cm sheet, and the second experiment was the exact same procedure in the transverse direction. Nine individual polymer samples were punched in order to make this possible. The resulting maps were cropped to show only the membrane and the immediate surroundings. The results of the longitudinal mapping are shown in figure 3.13, and the transverse mapping in 3.14. The constant scaling factor used in all calculations allows for direct comparison.

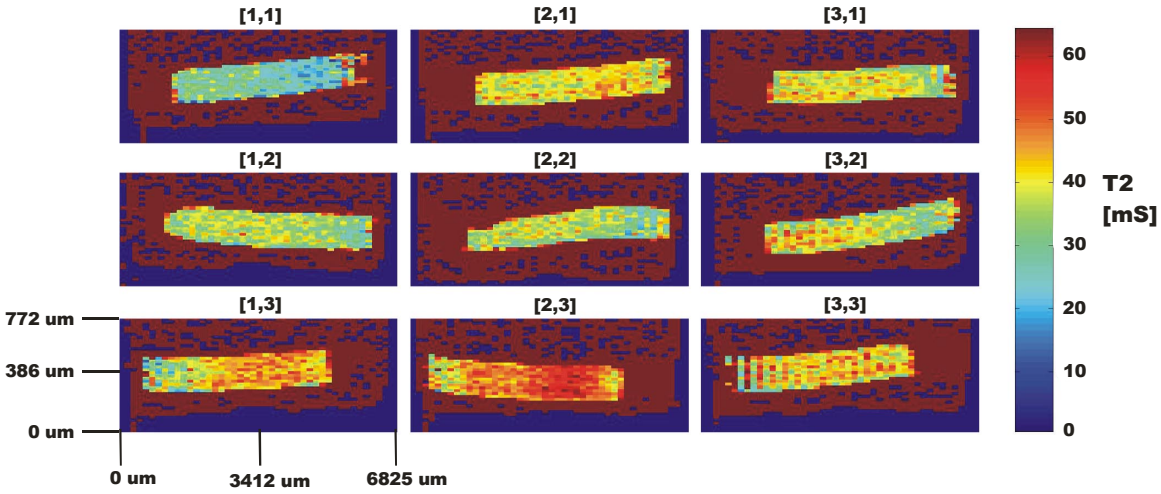


Figure 3.13. T_2 maps in the longitudinal direction for the material inhomogeneity experiment show that solvent T_2 values can vary significantly on both millimeter and 10 micron length scales. These images correspond to the punch scheme shown in figure 2.6.

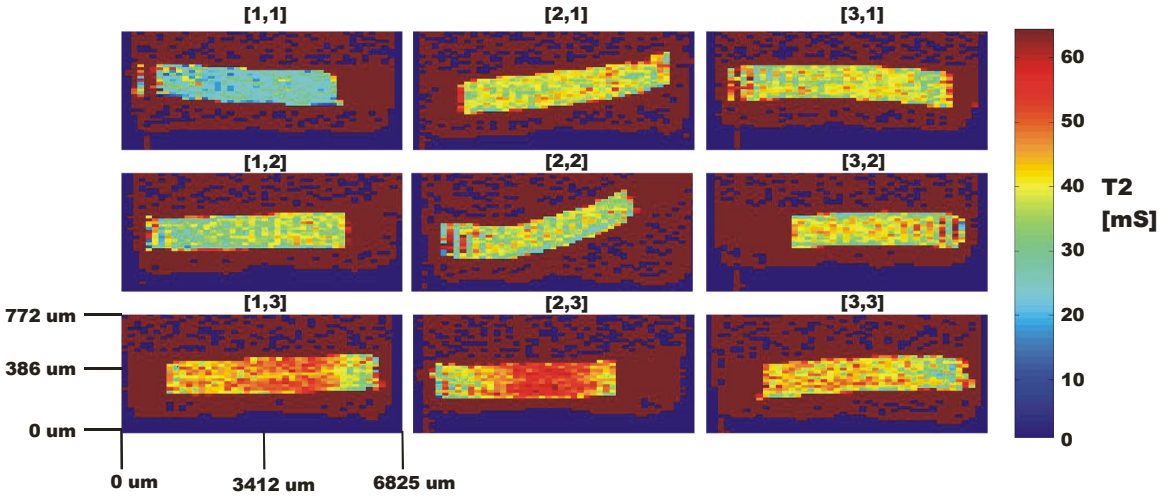


Figure 3.14. T_2 maps in the transverse direction for the material inhomogeneity experiment show that solvent T_2 values can vary significantly on both millimeter and 10 micron length scales. These images correspond to the punch scheme shown in figure 2.6.

As can be seen in figures 3.13 and 3.14 the level of molecular mobility variation is approximately equal in both directions, and the T_2 values within the membranes range from 20 ms in [1,1] to 60 ms in [2,3]. Since the samples are

only 5 mm in diameter this means that there is a molecular mobility difference equal to a factor of three in samples only 10 mm apart. In sample [1,3] the T_2 values range from 20 ms to 60 ms within the individual sample itself. This shows that the material inhomogeneity as measured by solvent molecular mobility is not confined to the millimeter length scale, but can vary significantly on a 20 micron length scale, which is the spatial resolution of these experiments. These heterogeneities account for the variations in T_2 and diffusion measurements at fixed methanol concentrations as shown in figures 3.4 and 3.9, respectively.

CONCLUSIONS

- The molecular mobility of the solvent within the polymer membrane increases as the concentration of the methanol solvent increases. This is due to increased solvent uptake and a consequent evolution of the membrane structure to exhibit a colloidal dispersion of micellar regions with larger channels or pores. Larger flow channels or pores correspond to a higher volume fraction of liquid within the polymer, and allow less restricted motion as seen in both the T_2 and diffusion experiments.
- Membrane swelling increases as the concentration of the methanol solvent increases. The quantitative measurement of the degree of swelling is dependent upon the measurement technique used. Using diffusion for contrast will result in smaller values of the measured thickness than using T_2 relaxation times for contrast. This is a result of T_2 measurements being sensitive to rotational diffusion of the spins which results in an interaction at the liquid/polymer interface and indicates a boundary layer of solvent in a restricted state relative to the free solvent.
- The measured diffusion coefficients of the liquid within the membranes agree with previous bulk studies of Nafion®-117.
- The T_2 relaxation times measured within a 3 cm by 3 cm square of Nafion®-117 exhibit differences equal to a factor of three on a 20 μm spatial scale. These spatial heterogeneities in molecular behavior may be

a factor in the premature failure of operational PEM fuel cell units, since membrane failure is usually localized and mechanical in nature. The more homogeneous the membrane, the more constant the proton transport through the polymer. Variations in the material will lead to variable transport, and this will reduce the efficiency of the fuel cell. In addition to reduced efficiency, the “hot spotting” of specific areas will lead to physical breakdown of the membrane and an overall failure of the fuel cell.

- The T_2 relaxation times of the liquid within separate samples prepared with the exact same chemical procedures varied by up to a factor of three. The procedure was never altered, but still showed variable results. This variation is explained by the material inhomogeneity of the material and the small size of the individual samples. The 5 mm size of the polymer sample resulted in a random sampling of the material inhomogeneities in the overall sheet.

LITERATURE CITED

[1] A.J. Appleby and F.R. Foulkes, “Fuel Cell Handbook”. Van Nostrand Reinhold Publications, New York (1989)

[2] J. Larminie and A. Dicks, “Fuel Cell Systems Explained”. 2nd Edition, Wiley Publications, West Sussex (2003)

[3] S. Srinivasan, R. Mosdale, P. Stevens, and C. Yang, *Annual Review of Energy and the Environment* **24** 281-328 (1999)

[4] S. Banerjee and D. Curtin, *Journal of Fluorine Chemistry* **125** 1211-1216 (2004)

[5] M. Rikukawa and K. Sanui, *Progress in Polymer Science* **25** 1463-1502 (2000)

[6] G. Gebel, *Polymer* **41** 5829-5838 (2000)

[7] L. Rubatat, A.L. Rollet, G. Gebel, and O. Diat, *Macromolecules* **35** 4050-4055 (2002)

[8] S. Slade, S.A. Campbell, T.R. Ralph, and F.C. Walsh, *Journal of the Electrochemical Society* **149** (12) A1556-A1564 (2002)

[9] S. Hietala, S. L. Maunu, and F. Sundholm, *Journal of Polymer Science* **38** 3277-3284 (2000)

[10] V. Barbi, S. Funari, R. Gehrke, N. Scharnagl, and N. Stribeck, *Polymer* **44** 4853-4861 (2003)

[11] W. Liu, K. Ruth, and G. Rusch, *Journal of New Materials for Electrochemical Systems* **4** 227-231 (2001)

[12] P. Mitra, P. Sen, and L. Schwartz, *Physical Review B* **47** (14) 8565-8574 (1993)

[13] B. MacMillan, A.R. Sharp, and R.L. Armstrong, *Polymer* **40** 2471-2480 (1999)

[14] B. MacMillan, A.R. Sharp, and R.L. Armstrong, *Polymer* **40** 2481-2485 (1999)

[15] M. Holz, *Chemical Society Reviews* **23** (3) 165-174 (1994)

[16] S. Heil and M. Holz, *Journal of Magnetic Resonance* **135** 17-22 (1998)

[17] A. Abragam, “The Principles of Nuclear Magnetism”. Oxford University Press, London and New York (1961).

[18] C.P. Slichter, “Principles of Magnetic Resonance”. Harper, New York (1963).

[19] P. Callaghan, “Principles of Nuclear Magnetic Resonance Microscopy”. Oxford University Press, Oxford (1991).

[20] S.L. Codd, “3DFT NMR Imaging of Solid-like Materials”. The University of Kent, Canterbury (September 1996).

[21] T.C. Farrar, “Introduction to Pulse NMR Spectroscopy”. The Farragut Press, Madison, WI (1997).

[22] M.D. Greenburg, “Advanced Engineering Mathematics”, Sections 11.3 and 11.4. Prentice Hall (1988).

[23] D.D. Traficante, *Concepts in Magnetic Resonance* **1** 73-92 (1989)

[24] E. Fukushima dn S.B.W. Roeder, “Experimental Pulse NMR: A Nuts and Bolts Approach”. Addison-Wesley (1981).

[25] J. Kida and H. Uedaira, *Journal of Magnetic Resonance* **27** 253 (1977)

[26] W.S. Price, H. Ide, and Y. Arata, *Journal of Physical Chemistry A* **107** 4784-4789 (2003)